# Characterisation of the readout circuit of an upgraded SiPM array for Xenoscope


by

Thomas Maher, thomas.maher@uzh.ch

supervised by

Prof. Dr. Laura Baudis, lbaudis@physik.uzh.ch
Dr. Ricardo Peres, rperes@physik.uzh.ch
Mariana Rajado Silva, mariana.rajado@physik.uzh.ch

Department of Physics

University of Zurich

September, 2024

**Abstract**

This thesis explores the development and characterisation of photosensor readout technology for astroparticle physics within the Xenoscope project at the University of Zurich. At the heart of Xenoscope is a dual-phase xenon time projection chamber (TPC), which is used for detecting subatomic particles and their interactions. The detector hosts a photosensor array composed of 192 VUV-sensitive silicon photomultipliers (SiPMs) from Hamamatsu Photonics, each with a $6 \times 6\,\mathrm{mm}^2$ active area, called a SiPM cell. These are loaded on to a printed circuit board (PCB) mounted with a pre-amplifier, which is responsible for amplifying the signals detected by the SiPM. The readout sums the signals from 16 SiPM cells to a single channel.

The project aims to increase the granularity of the current SiPM array. The goal is to individually read each $6 \times 6\,\mathrm{mm}^2$ SiPM cell. The upgrade includes experimenting with a more compact pre-amplifier, thus allowing for amplification of all 16 signals using a single PCB. New micro-coaxial cables are also incorporated to allow for compact signal readout and transmission. The performance of the entire readout circuit is evaluated, with particular focus on its effect on the signal pulses, which represent the electrical amplification of the detected photons.

The experimental tests are conducted in two setups: Sandbox, used for measurements at room temperature in a dark setting, and LArS, for measurements at cold temperature. These setups simulate the operational conditions of Xenoscope. The performance of the enhanced PCB are evaluated against the previously developed and implemented PCB under identical testing conditions.

The original PCB exhibited signals with less variance in amplitude for the same light intensity compared to the new PCB. Both the dark count rate (DCR) and crosstalk probability (CTP) values for the original and new PCBs were comparable, with DCR increasing proportionally with overvoltage and decreasing with temperature. The CTP increased similarly with overvoltage and tended towards zero at lower gains.

A comparison of gain as a function of overvoltage revealed minimal temperature dependence for both PCBs, as expected. A difference of approximately 10% in gain was observed between the original and new PCB, but still lying within the error margins of the analysis.

The original PCB has a better single-photon resolution (SPE), with a relative resolution between 4% and 8%, while the new PCB exhibited a SPE resolution varying from 8% to 22%, depending on temperature and bias voltage. A difference of 4% can be observed between the two PCBs for high gain.

Additionally, a ringing effect was observed in the waveforms of the 16-channel readout PCB, characterized by multiple smaller peaks following the primary signal peak. This is caused by increased current in the operational amplifiers (LTC6269-10), leading to reverse current through the amplifying resistor. Despite this, the integration of the compact pre-amplifier and micro-coaxial cables proved effective, enabling simultaneous readout of 16 signals. These results contribute to the ongoing improvements in enhancing the detection capabilities within the Xenoscope project.

Future work will include adding a capacitor in parallel to the feedback resistor on the op-amp to reduce the ringing effect at cold temperatures. Its effectiveness will be tested through further PCB characterizations for future measurements.

## Acknowledgements

I extend my sincere gratitude to Prof. Laura Baudis for providing me with the opportunity to join her research team, and participate in a leading direct dark matter search collaboration. My sincere thanks also go to Dr. Ricardo Peres and Mariana Rajado Silva for their consistent support and guidance, even during their busiest times. Their willingness to assist and always share a laugh made a significant difference. Special acknowledgment is due to Esteban, for his constant companionship and assistance with tasks such as transporting liquid nitrogen. Finally, I am grateful to my parents for their continued support throughout my Bachelor degree; and the whole research group, I very much appreciated your kindness and support throughout this thesis project.

# Contents

# 1 Introduction to Dark Matter Research: Methods and Objectives

Galaxies within our universe are spinning at such large velocities that the gravitational pull from their visible matter is not sufficient to keep them unified [1]; theoretically, they should have dispersed by now, a phenomenon also observed in galaxy clusters. This prompted researchers to propose the existence of an unseen, but interacting particle. They hypothesize the presence of an undetected substance that contributes with additional mass, thereby providing the necessary gravitational force to maintain the cohesion of these galaxies [2]. This substance has been named *dark matter*. The mystery surrounding the origins of dark matter represent a significant challenge in modern physics. Dark matter is distinct from ordinary matter because it does not interact through electromagnetic forces, meaning it does not absorb, reflect, or emit light, making it invisible. This makes it difficult to detect despite abundant evidence for its existence.

## 1.1 Evidence for Dark Matter

Dark matter was initially proposed in 1933 [1]. Subsequent years saw a growing body of evidence supporting its existence, propelled by advancements in astrophysical and cosmological observational techniques. The following sections detail key developments in dark matter research.

### 1.1.1 Coma Galaxy Cluster

In 1933, Fritz Zwicky investigated the dynamics of the Coma galaxy cluster using the virial theorem, a principle that relates the average kinetic energy of particles in a system to the system's gravitational potential energy [1]. Specifically, the virial theorem can be expressed as in equation (1):

$$2\langle K\rangle = -\langle U\rangle, \tag{1}$$

where $\langle K\rangle$ represents the system's average kinetic energy, and $\langle U\rangle$ is the average potential energy. By applying this theorem to the Coma cluster, Zwicky was able to estimate the total mass of the cluster based on the observed velocities of its galaxies.

Zwicky's analysis revealed a significant discrepancy: the visible matter in the form of galaxies within the cluster accounted for only a small fraction of the mass required to explain the observed velocities of this galaxy. In particular, the velocities suggested a higher total kinetic energy than what would be expected if only visible matter were contributing to the cluster's gravitational potential energy. This discrepancy can be further highlighted by considering equation (2) used to estimate the mass of the cluster from the observed velocities:

$$M_{\text{total}} = \frac{\sigma^2 R}{G}, \tag{2}$$

where $M_{\text{total}}$ is the total mass of the galaxy cluster, $\sigma$ is the standard deviation of the galaxies' velocities (a measure of their average speed), $R$ is the radius of the cluster, and $G$ is the gravitational constant. This equation shows that the total mass inferred from the galaxies' kinetic energy (via their velocities) far exceeds the mass of visible matter, because a higher $\sigma$ (indicative of higher velocities) implies a greater total kinetic energy among the galaxies. For instance, the total mass of the Coma cluster estimated using this method is about $4\times10^{13}$ solar masses, significantly higher than the visible mass, which is approximately $4\times10^{10}$ solar masses derived from the collective luminosity of the cluster's galaxies. This discrepancy indicates that the gravitational effects observed cannot be solely attributed to the visible matter, leading to the inference of additional, unseen mass.

### 1.1.2 Galactic Rotation Curves

In the 1970s, precise observations of the rotation curves of galaxies revealed a discrepancy that has become a cornerstone of the dark matter hypothesis [3]. These rotation curves, which show the velocity of stars against their distance from the galactic center, remained unexpectedly flat at large radii. This implied that the stars' orbital velocities did not decrease with distance from the center as would be anticipated if all the mass in the galaxy were visible. Instead, the flatness of the curves at large radii suggested that some form of unseen mass (dark matter) was present, exerting additional gravitational force.

The orbital velocity $v$ of stars orbiting a galaxy can be described by equation (3):

$$v(r) = \sqrt{\frac{GM(r)}{r}}, \tag{3}$$

where $G$ is the gravitational constant and $M(r)$ is the total mass enclosed within the radius $r$. The expected decrease in $v(r)$ based on visible matter alone is contradicted by the observed flat rotation curves. To address this difference, a model was introduced that includes a halo of dark matter. This halo's mass is crucial for explaining the constant rotational velocities across varying radii, suggesting $M(r)$ increases with radius well beyond the extent of luminous matter.

Figure 1 illustrates the characteristic flat rotation curve of a spiral galaxy, showing that the observed velocities of stars remain high even at large distances from the galactic center, a phenomenon not explainable solely by the gravitational pull of visible matter.

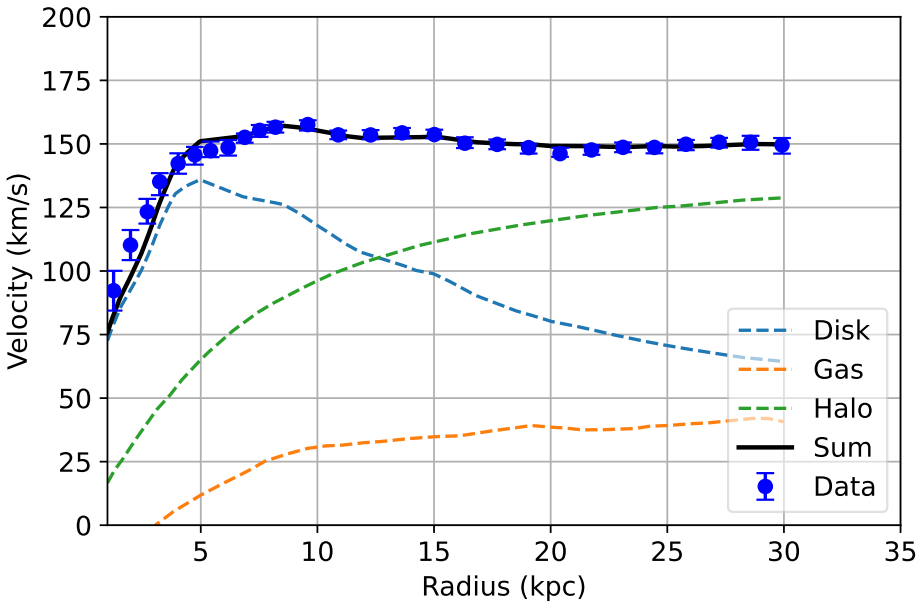


**Figure 1:** The rotation curve of galaxy NGC 6503. The plot shows the rotational velocity (in km/s) as a function of radius (in kpc) from the galactic center. The blue line represents the contribution from the disk, the green line represents the gas component, the red line indicates the dark matter halo contribution, and the black line is the sum of all components, which matches the observed data (shown as points). Figure adapted from [4]

### 1.1.3 The Bullet Cluster

The Bullet Cluster, known as 1E 0657-558, has been an important subject of study, yielding direct empirical evidence for the existence of dark matter [5]. This evidence came from the observation of a collision between two galaxy clusters, which allowed astronomers to separate the effects of visible matter, consisting mainly of hot gas detected via X-ray emissions, and dark matter, inferred from gravitational lensing measurements. Gravitational lensing occurs when a massive object, such as a galaxy cluster, bends the light from objects behind it due to its intense gravitational field, acting much like a lens. This bending effect can reveal the presence and distribution of mass, by the way it distorts the appearance of background galaxies. The key finding was that the gravitational potential revealed by lensing did not align with the distribution of hot gas, indicating that the majority of the mass within the cluster (presumed to be dark matter) was non-interacting and not visible.

In Figure 2, the two distinct colors represent different components of the galaxy clusters in the aftermath of their collision. The red color highlights the hot gas that emits X-rays, which is detected through X-ray observations. As the two clusters collided, this hot gas interacted with itself, therefore slowing down and becoming separated from the bulk of the mass in the clusters.

**Figure 2:** Composite image of the Bullet Cluster (1E 0657-558), showing the separation of hot gas (in red) and dark matter (in blue) following a cluster collision and thereby providing direct evidence for the existence of dark matter. Figure from NASA/CXC/SAO

The blue areas, on the other hand, map the distribution of dark matter. The presence of dark matter is inferred through gravitational lensing – the bending of light from distant galaxies as it passes through the gravitational field of the cluster. The blue color corresponds to the regions where gravitational lensing effects are strongest, indicating the presence of substantial mass.

It is clear from Figure 2 that the gravitational lensing effects (blue) do not coincide with the hot gas (red). If most of the mass were in the form of hot gas, we would expect the lensing to align with the red regions. This implies that most of the mass in the clusters is invisible and does not interact with the hot gas. This mass is attributed to dark matter, which passed through the collision without slowing down, unlike the hot gas. The separation between the hot gas and the inferred dark matter distribution in the Bullet Cluster is one of the most direct pieces of visual evidence for the existence of dark matter.

### 1.1.4 Cosmic Microwave Background

Following the exploration of dark matter through the Bullet Cluster, another compelling piece of evidence supporting the presence of dark matter comes from observations of the Cosmic Microwave Background (CMB). The CMB, a remnant from the early universe just 380,000 years post-Big Bang, encapsulates the oldest light in the universe, revealing the state of the universe when it became transparent to photons. Initially, the universe was a hot, dense "quark soup" of particles in thermal equilibrium. As it expanded, the interaction rates of particles decreased, leading to their eventual decoupling and freeze-out when their interaction rates fell below the universe's expansion rate. Approximately 105 years after the Big Bang, electrons and protons combined to form neutral atoms, thereby reducing the number of free electrons and making the universe transparent to photons.

The CMB is marked by minute temperature fluctuations of about 1 part in 100,000, a relic from the universe's early days. These anisotropies, observed as temperature variations, provide a large-scale structural map of the early universe as depicted in Figure 3. The angular power spectrum of these CMB anisotropies offers a detailed account of the early universe's composition by quantifying temperature variations across the sky against angular frequency. The precise measurements by the Planck satellite have been pivotal, particularly in determining the density of cold dark matter, which constitutes about 26% of the universe's mass-energy composition. The critical density ratio, calculated as:

$$\Omega_c h^2 = 0.120 \pm 0.001, \tag{4}$$

reflects this finding [6]. Here, $\Omega_c$ is defined as the ratio of the cold dark matter density $\rho_{CDM}$ in the present day Universe to the critical density $\rho_c$, which is given by:

$$\rho_c = \frac{3H_0^2}{8\pi G}, \tag{5}$$

where $H_0$ is the expansion rate of the universe at present, known as Hubble's parameter, and $G$ is the gravitational constant. The reduced Hubble parameter $h$ is defined as:

$$h = \frac{H_0^2}{100\text{km s}^{-1}\text{Mpc}^{-1}}. \tag{6}$$

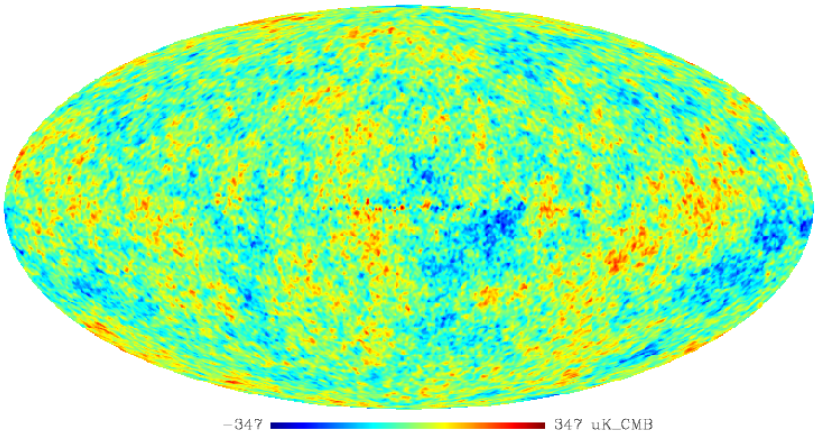


**Figure 3:** Map of the temperature fluctuations in the Cosmic Microwave Background, demonstrating the small-scale anisotropies that are essential in studying the structure and content of the early universe. The data used in this prediction is based on the WMAP 5-year data, showcasing a rich tapestry of temperature variations that help in deducing the presence and distribution of dark matter. Figure from [7].

## 1.2 Dark Matter Candidates

Despite its invisible nature, the gravitational effects of dark matter are evident in a variety of astrophysical and cosmological observations, suggesting that it constitutes about 85% of the total matter in the universe [8]. The quest to understand dark matter has led to the proposal of various candidates, each with its own theoretical motivations and implications for particle physics and cosmology.

Dark matter is not described by the Standard Model of particle physics, which describes the fundamental particles constituting ordinary matter, such as quarks, leptons, gauge bosons, and the Higgs boson. It is believed to be composed of new, undiscovered particles that are not accounted for in the Standard Model. Among the plethora of dark matter candidates, three main classes emerge: cold dark matter (CDM), hot dark matter (HDM), and warm dark matter (WDM). CDM candidates are typically slow-moving particles that were non-relativistic at the time of decoupling from the rest of the matter in the early universe [9]. This category includes Weakly Interacting Massive Particles (WIMPs), axions [10], and sterile neutrinos [11]. WIMPs are one of the most extensively studied candidates because of the possibility of detection via direct and indirect methods. On the other hand, HDM candidates are particles that move at relativistic speeds. Neutrinos are a classic example of HDM. They decoupled from the hot plasma of the early universe when temperatures fell below around 1 MeV. From that point, they traveled at speeds close to the speed of light. The high thermal velocities of neutrinos inhibited their ability to cluster together under gravitational forces on small scales, causing the neutrino density to remain relatively uniform and smoothing out any small-scale density peaks or fluctuations, leading to a "top-down" formation of structures where large superclusters would form first, followed by fragmenting into smaller structures like galaxies, which is the opposite of the "bottom-up" sequence. In addition, WDM, with particle velocities slower than HDM but faster than CDM, represents a middle ground. WDM, such as keV-mass sterile neutrinos, could also contribute to structure formation, potentially smoothing out smaller structures without preventing the formation of galaxies, thus offering a hybrid scenario in cosmic evolution [12].

However, observations of the cosmic structure favor a "bottom-up" scenario, where smaller objects like stars and galaxies formed first and then merged to create larger structures. The evidence thus suggests that dark matter is predominantly "cold", consisting of slower-moving particles that do not erase these small-scale structures, aligning with the currently accepted cosmological model of structure formation [11].

### 1.2.1 WIMPs

As mentioned above, WIMPs are proposed particles that are considered one of the leading candidate types for dark matter. The defining characteristics of WIMPs include their substantial mass, which makes them "cold" (non-relativistic at the time of galaxy formation), and their weak interaction with ordinary matter, except through gravity [13]. These properties allow WIMPs to be pervasive throughout the cosmos without disrupting the observed structures of galaxies and the cosmic microwave background radiation.

Observations of distant galaxies today, as well as evidence from earlier epochs of the Universe,

suggest a consistent relic density of dark matter. This constancy can be traced back to the Universe's conditions shortly after the Big Bang. When the Universe's temperature was significantly higher than the mass of WIMPs ($T \gg m_\chi$), WIMPs were very abundant [14]. As the Universe cooled to temperatures below the mass of the WIMPs ($T < m_\chi$), the rate of WIMP annihilation exceeded their formation, declining exponentially with $\exp(-m_\chi/T)$ until a point known as "freeze-out" was reached, beyond which the abundance of WIMPs remained unchanged [15].

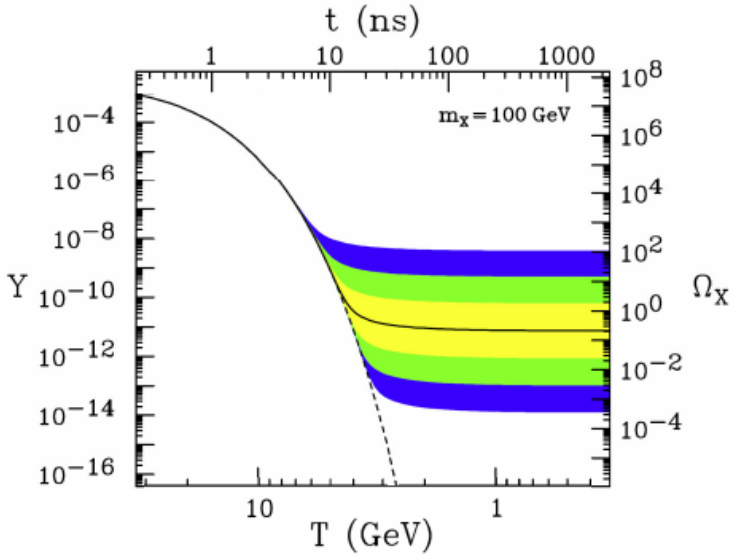


**Figure 4:** Comoving number density $Y$ and thermal relic density $\Omega_X$ of a 100 GeV WIMP, shown as functions of temperature $T$ and time $t$. The solid line marks the stabilization at the observed relic density, with shaded regions indicating variances by factors of 10, $10^2$, and $10^3$. Figure from [15].

The relic density of dark matter is closely linked to the WIMP cross-sections. These cross-sections are important for determining the stable mass density of WIMPs observed today. Such estimations support the consistency of dark matter density from the early universe to the present, substantiating the thermal freeze-out models of WIMP behavior [16].

WIMPs arise naturally in several theories beyond the Standard Model of particle physics, such as supersymmetry and extra-dimensional theories [17]. The appeal of WIMPs lies in their ability to be integrated into the existing frameworks of particle physics while simultaneously addressing the astrophysical and cosmological evidence for dark matter.

## 1.3 Detection Techniques

Three main strategies are used to study dark matter. Direct detection aims to identify dark matter particles through their interactions with ordinary matter in sensitive detectors, capturing the faint signals that would be produced. Indirect detection looks for the secondary

products, like gamma rays, neutrinos, and cosmic rays, that emerge from dark matter particles' annihilation or decay. The third approach, the production method, attempts to generate dark matter particles in controlled settings such as particle accelerators, observing the results of collisions to infer on the existence of dark matter.

- **Direct Detection:** Direct dark matter detection involves using specialized detectors on Earth to search for signs of dark matter. The theory is based on the assumption that, as the Earth travels through the galaxy's dark matter halo, interactions between dark matter particles and the atoms in the detectors will occur, generating detectable signals.

  These scattering events within detectors would lead to a kinetic energy transfer to the nuclei, causing the nuclei to recoil, an action that is central to detecting the presence of dark matter [18, 19].

  One of the detection methods requires the use of cryogenic detectors [19]. These function at temperatures typically below 100 mK. Such low temperatures enable the measurement of phonons, which are quantized vibrational modes produced when a nucleus recoils following an interaction with a particle. This technique is effective for detecting events with very low energies.

  Some detectors capture the ionization or scintillation signals generated when a dark matter particle collides with the detector's material. Ionization detectors track the electrons dislodged by the recoiling nucleus, whereas scintillation detectors record the light released when atoms within the detector are excited to a higher energy state, which then decay by photon emission [20].

  Another key category is dual-phase detectors, typically utilizing noble gases like xenon. These detectors are capable of simultaneously measuring both scintillation light and ionization charge from a single event. This combined detection technique enhances the ability to distinguish dark matter interactions from background noise, thus increasing the detection accuracy [20].

  A major obstacle in detecting dark matter directly is differentiating possible dark matter signals from background events, which may originate from cosmic rays, natural radioactivity, and other environmental factors. To mitigate this, detectors are situated deep underground and are built using extremely pure materials to reduce external interference. The most sensitive experiments employ techniques for removal of impurities within the target material. In addition, such experiments record at least two different signal types (such as ionization and phonons) from each interaction. This helps distinguish nuclear recoil events, which are probable indicators of dark matter, from electron recoil events, which are typically associated with background disturbances.

- **Indirect Detection:** Indirect dark matter detection focuses on identifying byproducts of dark matter interactions, such as their annihilation or decay into Standard Model particles like photons, neutrinos, and cosmic rays. Such interactions are predicted to occur in dense cosmic structures like the center of galaxies, or the Sun, making these locations focal points for indirect detection strategies [21, 22].

Indirect detection identifies unusual levels of Standard Model particles, potentially indicating dark matter, by using air shower arrays, gamma- and X-ray telescopes, neutrino telescopes, and particle detectors on balloons or satellites [21]. A key challenge is distinguishing dark matter signals from astrophysical backgrounds, which requires advanced statistical and computational methods [23].

- **Production:** Production methods for detecting dark matter involve generating dark matter particles in highly controlled settings and subsequently analyzing the interactions or decay outcomes of these particles. This technique is mainly conducted in high-energy physics facilities, such as the Large Hadron Collider (LHC) at CERN [24].
- **Production:** Production methods for detecting dark matter involve generating dark matter particles in highly controlled environments and analyzing the results of their interactions or decay outcomes. This technique is primarily employed in high-energy physics facilities, such as the Large Hadron Collider (LHC) at CERN. In colliders, dark matter particles themselves are not directly observable because they do not interact electromagnetically or strongly, and thus do not leave tracks in detectors. Instead, their presence is inferred through the measurement of missing energy and momentum in particle collisions [24]. When particles collide, dark matter particles may be produced alongside visible particles. By precisely measuring the energy and momentum of the visible particles and comparing these to the total energy and momentum before the collision, one may identify discrepancies. A significant amount of missing energy and momentum can indicate that some other particles, presumed to be dark matter, were produced in the collision but escaped detection. This method relies on the conservation of momentum and energy.

# 2 DARWIN: The Ultimate Dark Matter Detector

DARWIN (DARk matter WImp search with liquid xenoN) represents a significant leap forward in the search for dark matter. As a next-generation experiment, DARWIN will employ a liquid xenon (LXe) time projection chamber (TPC) to detect WIMPs. With its unprecedented sensitivity, DARWIN is poised to probe a wide range of WIMP masses and cross-sections with the goal of uncovering the elusive nature of dark matter [25]. The leading experiments at the moment are the XENONnT [26] experiment and the LUX-ZEPLIN (LZ) [27] experiment. In 2021, the XENON/DARWIN and LZ collaborations formed the XLZD consortium [28]) to develop DARWIN/G3, a next-generation observatory combining XENONnT and LZ technologies to achieve unprecedented sensitivity by scaling up detector size, minimizing backgrounds, and enhancing purification systems.

## 2.1 Dual-phase xenon time projection chambers

The core of the DARWIN detector will be a dual-phase TPC containing a large volume of liquid xenon. This design aims to maximize the efficiency of detecting rare interactions that might indicate the presence of WIMPs. The detector is to be located underground and surrounded by a series of concentric shielding structures to minimize background events and therefore enhance the sensitivity of experiment to rare events. One potential underground site are the halls of the Laboratori Nazionali del Gran Sasso (LNGS). Shielded by 1400 m of rock (equivalent to 3400 m of water), the LNGS provides exceptional protection against cosmic rays. Dual-phase TPCs are central to several leading direct dark matter detection experiments, such as XENONnT [26], LUX-ZEPLIN [27] or PandaX-4T [29].

In these detectors, interactions between a particle and a xenon atom can lead to either a nuclear or an electronic recoil. A nuclear recoil occurs when an incident particle, such as a WIMP or a neutron, elastically scatters off the nucleus of a xenon atom. On the other hand, an electronic recoil occurs when an incident particle, such as a gamma ray or an electron, interacts with the electron clouds of the xenon atoms. In this case, the particle transfers energy to the atomic electrons, causing them to be ejected from the atom or excited to higher energy levels.

This interaction there ionizes and excites the xenon atom, which then pairs with another xenon atom to form a transient $Xe_2$ excimer [30]. Some of the energy converted into heat and lost to the system. The excimer emits a 175 nm photon upon returning to the ground state. These photons, which do not excite further xenon atoms, travel through the xenon and are detected by photosensors positioned at the top and bottom of the chamber. The chamber's walls are designed to effectively reflect these photons, enhancing their detection. The initial detection of these photons is referred to as the S1 signal, as shown in Figure 5.

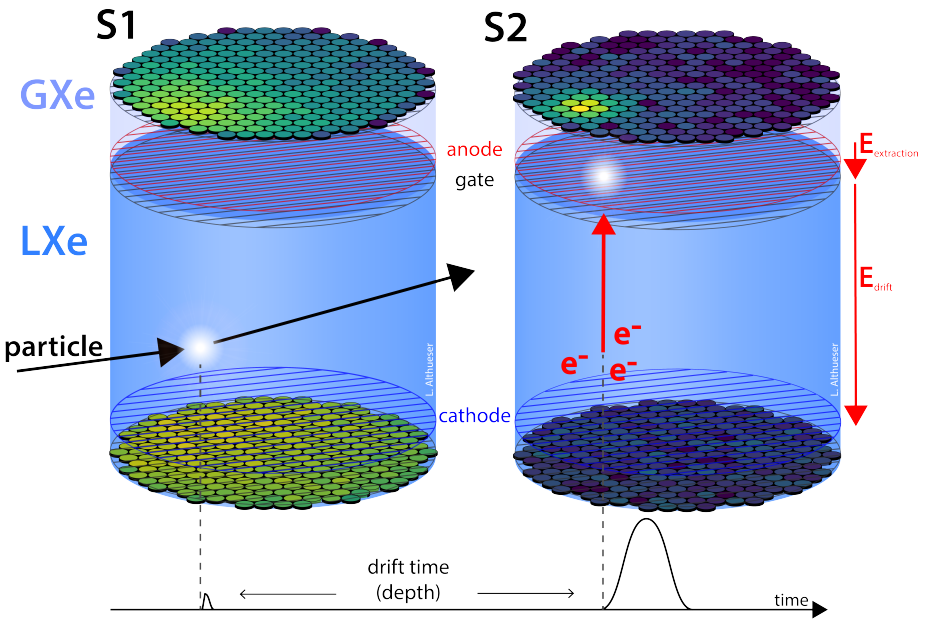


**Figure 5:** The operation principle of a two-phase xenon TPC. A particle interaction in liquid xenon gives rise to a prompt scintillation signal S1 and a delayed, amplified proportional scintillation signal S2. Figure taken from L. Althüser/XENON collaboration.

In dual-phase TPCs, the interaction with xenon atoms also leads to the release of free electrons from the atoms. These electrons are subjected to an electric field, denoted as $E_{\text{drift}}$, causing them to drift upwards. Upon reaching the gate, a grounded stainless steel mesh, the electrons encounter a significantly stronger electric field, $E_{\text{extraction}}$, situated between the gate and the anode meshes. As the electrons move between the gate and the anode, they cross the liquid-gas interface. The $E_{\text{extraction}}$ field prompts additional scintillation in the gas phase, resulting in the emission of 175 nm photons once more. These photons are captured and constitute the secondary signal, referred to as S2.

The energy scale equation used to quantify this is given by eqaution (7) [31]:

$$E = W(n_y + n_e) = W\left(\frac{S_1}{g_1} + \frac{S_2}{g_2}\right), \tag{7}$$

where $W \approx (13.7 \pm 0.2)\,\text{eV}$ [32] is the energy required to produce an excited or ionized xenon atom. $n_y$ represents the number of photons emitted during the excimer de-excitation and electron-ion pair recombination processes, while $n_e$ is the number of electrons that escape recombination. The scaling constants $g_1$ and $g_2$ represent the gain factors for the S1 and S2 signals, respectively. From the S1 and S2 the number of photons and electrons can be inferred and the energy of the interaction reconstructed.

Even when reflected, the photons are detected almost immediately, and the time difference

between the S1 and S2 signals depends exclusively on the electrons' drift time. This drift time is influenced by the strength of the electric field and the location within the chamber where the recoil occurred. The method for position reconstruction utilizes this time difference to calculate the $z$ coordinate of the recoil directly given the measured drift velocity. The $x$ and $y$ coordinates are determined by the pattern formed by the photosensors in the top array when they detect the light from the extraction of the S2 signal.

Depending on whether the signals originate from electronic or nuclear recoils, variations in the characteristics of the observed signal, particularly the width and amplitude of the secondary scintillation signal S2, are noted. By analyzing the relative magnitudes of the primary S1 and secondary S2 scintillation signals, it is possible to discern the type of interaction, differentiating between electronic and nuclear recoils [33].

## 2.2 Sensitivity and Expected Reach of Direct Detection Experiments

DARWIN has been designed to investigate the experimentally accessible parameter space for WIMPs across a broad mass spectrum, ranging from as low as $5\,\mathrm{GeV/c^2}$ to more than $10\,\mathrm{TeV/c^2}$, through spin-independent and spin-dependent scattering [34]. DARWIN will utilize 40t of liquid xenon (LXe) target. DARWIN's sensitivity to WIMP-nucleon interactions is illustrated Figure 6, which show the expected cross-sections over a range of WIMP masses for several direct detection dark matter experiments.

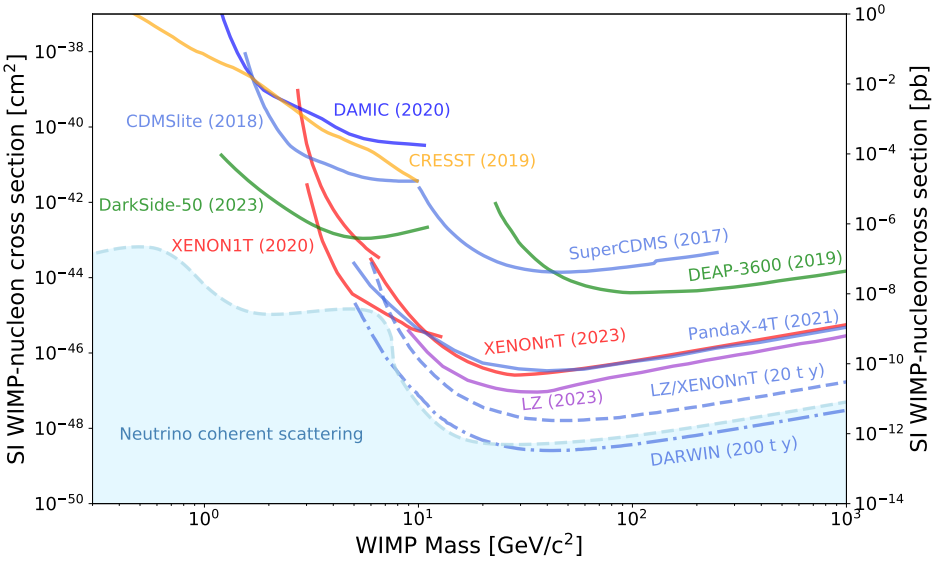


**Figure 6:** Spin-independent WIMP-nucleon cross-section as a function of WIMP mass, ranging from 1 to $1000\,\mathrm{GeV}/c^2$. The plot includes current limits from multiple experiments such as XENONnT (2023), LZ (2023), among others sensitivity projections for DARWIN (200 t y projection) [35].

Spin-independent (SI) scattering involves interactions where the scattering cross-section is independent of the spin orientations of both the dark matter particle and the target nucleus

or electron. In SI interactions with nuclei, the cross-section is coherently enhanced by the square of the nuclear mass number $A$, which increases sensitivity in heavier targets. SI scattering is commonly the main focus in direct detection experiments such as XENONnT [26, 36].

For spin-dependent (SD) scattering interactions, the scattering amplitude is influenced by the relative spin orientations of the dark matter particle and the target nucleus or electron. For SD scattering on nuclei, the interaction primarily involves the net nuclear spin, contributed by unpaired nucleons. Although SD cross-sections are generally smaller than those of SI, they remain crucial for probing certain dark matter models.

The increased volume of LXe allows for probing lower bounds of WIMP-nucleon cross-sections. With an exposure of approximately 200 ton-years and ultra-low background conditions, DARWIN is expected to achieve sensitivity to spin-independent WIMP-nucleon interactions with a cross-section as low as $1.4 \times 10^{-48}$ cm$^2$ for a WIMP mass of 50 GeV/c$^2$ at a 90% confidence level. This represents an improvement of more than an order of magnitude over the current best limit established by XENONnT [37]. With an exposure of $1.09 \pm 0.03$ ton-years, XENONnT sets the leading limit on blind analysis search for DM with a spin-independent WIMP-nucleon cross section of $2.58 \times 10^{-47}$cm$^2$ for a WIMP mass of 28 GeV/c$^2$ at 90% confidence level [38].

For a 50 GeV/c$^2$ WIMP, DARWIN's expected median discovery significance is projected to surpass $3\sigma$ ($5\sigma$) for cross-sections greater than $2.6 \times 10^{-48}$ cm$^2$ ($5.0 \times 10^{-48}$ cm$^2$). [37] The anticipated sensitivity for spin-dependent WIMP coupling to neutrons is $2.2 \times 10^{-43}$ cm$^2$ and $6.0 \times 10^{-42}$ cm$^2$ for protons [37]. Thanks to its low background and significant mass, DARWIN will be capable of exploring dark matter interactions down to the irreducible neutrino background, commonly referred to as the "neutrino fog" [34].

### 2.3 Xenoscope: A full-height DARWIN Demonstrator

Xenoscope is a project developed at the University of Zürich. It features a 2.6-meter-tall dual-phase LXe TPC, which matches the height projected for the DARWIN experiment. The primary goal of Xenoscope is to validate the drift of electrons across the entire 2.6 m span within the detector. This is achieved by either using a radioactive source, which will trigger events inside the TPC, or by illuminating a photocathode at the chamber's base by a pulse from a xenon lamp. A xenon lamp is a type of lamp that produces light by passing an electric current through ionized xenon gas contained within a glass bulb. The pulse from the lamp then releases electrons from the photocathode that must traverse the LXe. As some electrons get trapped by impurities as the cloud drifts upwards, a xenon purification system in used in the circulation loop of the detector to minimize their presence.

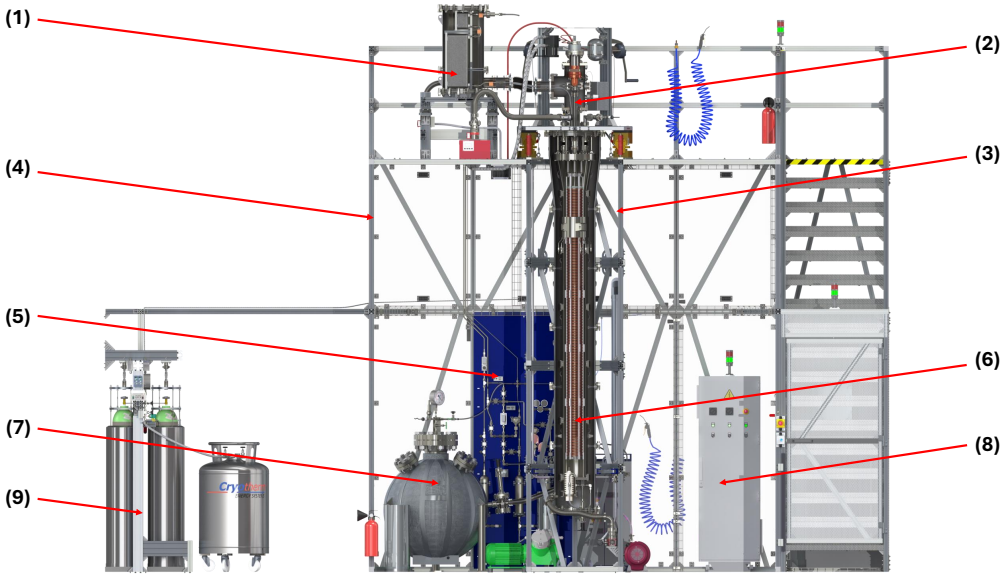


**Figure 7:** Schematic view of the Xenoscope facility with the 2.6 m TPC installed in the cryostat. Legend: (1) heat exchanger, (2) cooling tower, (3) inner frame, (4) outer frame, (5) purification gas panel, (6) TPC in the 24.8 cm diameter and 312 cm height cryostat, (7) high-pressure storage vessel of liquid recovery system, (8) power distribution cabinet, (9) gas recovery and storage system. Figure adapted from [39].

Xenoscope has a capacity of up to approximately 400 kg of liquid xenon [39]. The TPC is structured with 173 copper ring electrodes along its 2.6 m and is interconnected by PTFE insulators. It features a cylindrical volume filled with liquid xenon and a thin layer of gaseous xenon at the top. Positioned just above the liquid-gas interface, the top array photosensors comprises 48 Hamamatsu VUV4 SiPM (model S13371-6050CQ-02) organized in a 12-channel readout to efficiently detect secondary scintillation S2 signals [40].

The target circulation speed is a flow rate of 70 standard liters per minute and an operational electric field strength of around 200 V/cm [39]. The purity level of the xenon is deduced from the *electron lifetime*, the duration over which the number of electrons is reduced by a factor of $e$ due to impurity attachment. High xenon purity is indicated by a large electron lifetime, suggesting successful electron transport through the LXe.

The target circulation speed is a flow rate of 70 standard liters per minute and an operational electric field strength of around 200 V/cm [39]. The purity level of the xenon is deduced from the *electron lifetime*, the duration over which the number of electrons is reduced by a factor of $e$ due to impurity attachment. High xenon purity is indicated by a large electron lifetime, suggesting successful electron transport through the LXe. The electron lifetime is reported to be $664 \pm 23$ $\mu$s, determined by continuous purification of the liquid xenon. Factors affecting electron lifetime include the purification flow rate, impurity concentration, electric field strength, and temperature.

The goal to observe a full 2.6-meter electron drift was approached in stages. Initially, a purity monitor within the LXe with a 525 mm drift length was employed for early electron lifetime assessments [41]. Then, the setup was scaled to encompass the entire 2.6 meters as a dual-phase TPC.

## 2.4 The Top SiPM Array of Xenoscope

Situated just above the liquid-gas interface of the TPC, the top array of photosensors plays a critical role in detecting secondary scintillation (S2) signals. This array is composed of 48 Hamamatsu VUV4 SiPMs (model S13371-6050CQ-02), organized into 12-channel readouts to optimize S2 signal detection. An image of the SiPM array is shown in Figure 8, illustrating its precise configuration.

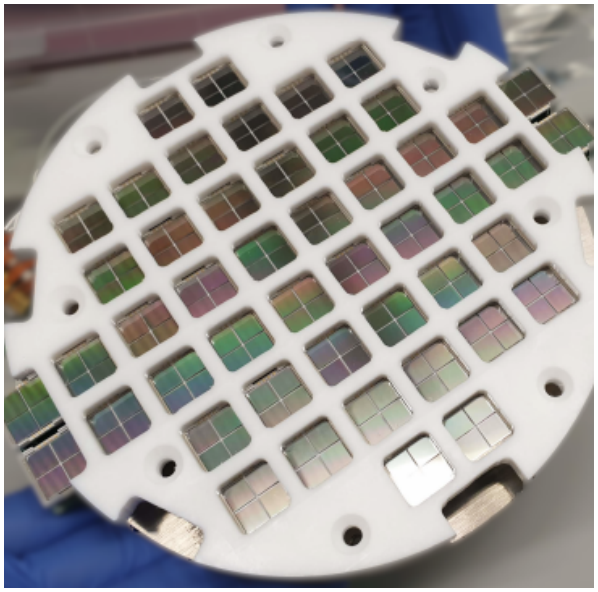

**Figure 8:** The SiPM array installed in the Xenoscope, detailing the arrangement of the SiPMs.

The array features 192 SiPM units, each 6×6 $mm^2$, configured into 2×2 quad modules, resulting in a total sensitive area of 12×12 $mm^2$ per module. Mounted on printed circuit boards as units called "tiles," these 12 tiles are crucial in facilitating enhanced VUV light detection. Each quad module includes four channels, encompassing a photosensitive area of 5.9 mm × 5.85 mm with 13,923 pixels and a 60% geometrical fill factor [40].

The tiles, beyond providing mechanical support, also distribute voltage and amplify signals using OPA847 op-amps for a 20-fold increase in the summed SiPM signals, thus reducing power consumption and heat generation. Specialized tiles are equipped with PT100 sensors for monitoring temperature, ensuring operational stability and mechanical security through a robust attachment to the TPC via a stainless steel plate and grooved PAI pillars secured with screws beneath a perforated PTFE cover.

# 3 Silicon Photomultipliers

This chapter will provide a detailed theoretical background of the SiPM. The subsequent subsections will offer an overview of silicon-based photodetectors, focusing on the avalanche photodiode (APD) and SiPM technologies.

## 3.1 Silicon Light Sensors

A silicon crystal, when in its pure state, has a balanced charge, making it resistant to electrical flow. Altering this balance by doping creates a PN junction: N regions are doped with electron donors and P regions with hole donors, facilitating free movement of electrons and holes [42].

When a P-type semiconductor, characterized by an excess of holes, is combined with an N-type semiconductor, which has an excess of electrons, a natural diffusion of charge carriers occurs across the junction due to the existing concentration gradients. Specifically, electrons from the N-side migrate into the P-side, while holes from the P-side move to the N-side. As electrons leave the N-side, they leave behind positively charged donor ions, and similarly, as holes leave the P-side, negatively charged acceptor ions remain. This exchange results in a depletion region near the junction, characterized by a lack of mobile charge carriers but filled with fixed charged ions [43].

The accumulation of positive ions on the N-side and negative ions on the P-side generates an electric field across this depletion region, positioning the N-side at a higher potential relative to the P-side. This electric field acts to counter further diffusion of charge carriers across the junction. At equilibrium, the diffusion current, which us driven by concentration gradients, is precisely balanced by the drift current, which is driven by the built-in electric field. This built-in field effectively sweeps electrons back towards the N-side and holes towards the P-side, thus preventing any additional net diffusion of charge carriers across the junction [43].

Silicon light sensors, based on PN-junctions, activate when photons enable electrons to move from the valence to the conduction band, creating an electron-hole pair. This movement, guided by the electric field, results in a photocurrent when connected through an external circuit. Therefor, the photocurrent can be measured to infer if a photon has interacted in the PN-junction, creating a basic photodetector.

## 3.2 Avalanche Photodiodes

The APD is built on a positive-intrinsic-negative (PIN) diode structure, which consists of p-n diodes separated by an intrinsic semiconductor region, the term *intrinsic* denotes a segment of semiconductor material that lacks intentional doping with impurities to classify it as n-type or p-type; it remains fundamentally undoped [43]. This intrinsic section is crucial to the functionality of the photodiode, serving as a zone where electron-hole pairs, generated by photons, are effectively gathered. Commonly to enhance the space charge distribution, an additional p-region is introduced between the $i$ region and the n-region, creating a peak in the electric field at the pn-junction.

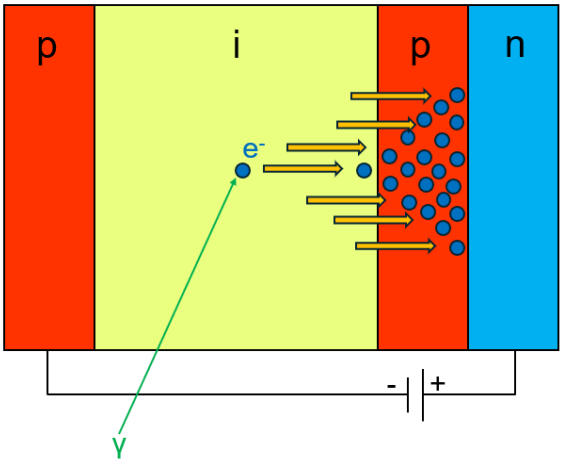


**Figure 9:** Schematic of the APD working principle. A photon leads to the release of an electron via the photoelectric effect, which then causes an avalanche by impact ionization.

The APD is divided into two main areas: the absorption region $i$ and the multiplication region (pn-junction), with the i-region being significantly larger to maximize photon detection. When a photon enters the absorption region, it generates an electron-hole pair through the photoelectric effect. The applied voltage causes the hole to migrate to the p-region, and the photoelectron to the multiplication region. Within the i-region, the electric field is relatively weak but increases as it approaches the pn-junction. Upon reaching the highly doped p-region, the electric field intensifies sharply, propelling electrons towards the n-region. Here, impact ionization occurs, moving valence electrons to the conduction band. If an electron does not have enough initial energy, it recombines back into the valence band.

The operational voltage of the APD dictates whether an electron remains in the conduction band post-collision. At sufficiently high voltages, each collision results in the release of an additional electron into the conduction band, initiating further impact ionization. This exponential increase in electron numbers, known as avalanche breakdown, significantly amplifies the signal.

The term *gain* refers to the total number of electrons generated during the avalanche process. It depends on equation (8):

$$G = \frac{q_f}{q_i}, \tag{8}$$

where $q_f$ is the final charge, $q_i$ is the initial charge, and $G$ is the gain.

This gain reaches a point of saturation where further increases in voltage do not enhance the gain. An APD operating at a voltage that causes all available valence electrons to move to the conduction band enters what is known as Geiger-mode. The minimum voltage required to achieve Geiger-mode is termed the breakdown voltage (BV). Further, the gain increases as the applied reverse bias voltage rises.

## 3.3 Silicon Photomultipliers

Silicon photomultipliers (SiPMs) represent a class of solid-state photodetectors capable of detecting and amplifying single photons. A SiPM comprises an array of APDs arranged in parallel on a silicon substrate, with each APD operating above its breakdown voltage in Geiger-mode. When a photon interacts with the active area of an APD, it generates an electron-hole pair. The intense electric field present in the depletion region initiates an avalanche multiplication of this charge carrier, producing a substantial number of electron-hole pairs (typically $10^5 - 10^6$). This amplified charge pulse is then recorded as a digital output signal [44].

SiPMs are regarded as counting devices due to their parallel structure and operating principle. As mentioned they consist of numerous APDs operating in Geiger mode, arranged in parallel on a silicon substrate. The microcells respond in a binary manner: they either fire upon detecting a photon or remain inactive. The SiPM's output is a sum of the signals from all triggered microcells, and its amplitude is proportional to the number of detected photons, giving it photon-counting capability. The SiPM's pixel saturation is determined by the number of microcells; it accurately counts photons as long as their number remains below the available microcell count. However, if the photon count exceeds the microcell capacity, the device saturates, and the output no longer reflects the exact number of photons [45].

To control the avalanche current and reset the APD post-avalanche, each APD is series-connected with a quenching resistor. The quenching resistor controls the avalanche current in each microcell by limiting its flow. When an incoming photon triggers an avalanche breakdown in a microcell, the quenching resistor, connected in series, restricts the current during this process. This current flow creates a voltage drop across the resistor, reducing the bias voltage below the breakdown level and stopping the avalanche. The microcell capacitance then discharges through the resistor, allowing the bias voltage to recover in a process called recovery time. Without this resistor, the current could continue indefinitely, damaging the microcell. This configuration enables the SiPM to detect additional incoming photons.

### 3.3.1 Characteristics of the SiPM

The Silicon Photomultiplier (SiPM) has several key characteristics that define its performance and suitability for various applications. These include:

- **Breakdown Voltage (BV):** The voltage at which the SiPM starts to operate in Geiger-mode.
- **Gain:** The amplification factor of the SiPM, indicating how much the initial charge signal is increased, as described in equation (8).
- **Dark Count Rate (DCR):** In a dark environment SiPMs can still produce signals, so-called dark counts. Thermal activity can cause electrons to move to the conduction band, leading to detectable signals by the SiPMs. These pulses are indistinguishable from those generated by an incident photon. The dark counts can be misinterpreted as a physical event, so a high DCR is problematic for event searches. This issue has been a notable disadvantage of SiPMs compared to traditional Photomultiplier Tubes

(PMTs), with recent SiPM models exhibiting dark count rates that are still about 80 times higher than those of PMTs [46]. This is also the reason why PMTs are the main photosensor choice for the current generation of dark matter detectors.

DCR is generally expressed in kHz/mm$^2$ or MHz/cm$^2$ and varies based on factors like operating temperature, overvoltage (additional bias beyond breakdown voltage), and the quality of the silicon used. At a standard room temperature of about 25°C, typical DCR values for contemporary SiPMs lie between several hundred kHz/mm$^2$ to a few MHz/mm$^2$, with variations depending on the manufacturer and specific device characteristics. For example, the VUV-sensitive Hamamatsu S13360 series, used on the photosensor array of Xenoscope, exhibits a DCR of 100 kHz/mm$^2$ at 25°C [44].

The DCR notably increases exponentially with temperature, essentially doubling with every 8-10°C increment. This rise is attributed to the increased thermal generation of charge carriers within the silicon lattice.

For instance, at 170 K, the DCR for the Hamamatsu S13360 series plummets from 100 kHz/mm$^2$ at 25°C to merely 0.1 Hz/mm$^2$, marking a reduction of more than six orders of magnitude [47].

- **Single Photon Resolution (SPE Resolution):** It is the ability of the device to distinguish between the electrical signals produced by the detection of individual photons. High SPE resolution means the SiPM can accurately count and resolve the number of photons that interact with it, which is crucial for applications where the precise measurement of light intensity is necessary, such as low-light imaging or photon counting experiments. Contrary to traditional PMTs, SiPMs can have an SPE resolution of around 4%, which is much smaller compared to the PMTs resolution of around 20% - 30%. A SiPM with excellent SPE resolution will produce distinct and separable signal peaks for each photon detected, enabling accurate photon counting and minimizing the overlap between signals that could lead to inaccuracies in photon quantification.

- **Crosstalk Probability (CTP):** Crosstalk in an array of pixels happens when an electron, after being excited into the conduction band in one pixel, collides with the lattice structure and generates a secondary photon. This new photon, upon striking an adjacent pixel, can initiate an additional avalanche event. The likelihood of such crosstalk occurrences is quantitatively described by the crosstalk probability (CTP), which is the ratio of crosstalk incidents to the number of detected dark counts. A detailed discussion on how the CTP is calculated can be found in Section 5.2.2.

- **Afterpulses:** Afterpulses are a form of correlated noise in SiPMs that can degrade their performance, especially in low-light or single-photon detection applications. Afterpulses occur when charge carriers (electrons or holes) from the initial avalanche, which was triggered by a photon or dark count, get temporarily trapped in defect sites in the silicon lattice. During the recharge phase of the SiPM microcell, these trapped carriers can be released after some delay ranging from nanoseconds to microseconds. If the released carrier reaches the high-field region, it can potentially trigger a second, delayed avalanche in the same microcell, causing an afterpulse [48].

# 4 Characterisation of the SiPM Readout

This chapter describes the experimental setup, followed by an explanation of the data acquisition process and presentation of the results. For the experimental comparison, two printed circuit boards (PCBs), which are responsible for the signal readout, were tested: one employing the operational-amplifier OPA847 and the other using one which had not been tested yet, operational-amplifier LTC6269-10, enabling an analysis and discussion of any discrepancies observed in the results.

## 4.1 The Setups

There were two experimental setups used for the characterisation of the SiPMs. One established a dark environment at room temperature, called Sandbox. Here, first tests were made ensuring the functionality of the PCBs. The other system, the Liquid Argon Setup (LArS), also ensures cooling of the environment using liquid nitrogen. The following section will provide further details about these two systems.

The SiPM utilized in this study has dimensions of $6 \times 6\,\mathrm{mm}^2$ and is mounted onto a PCB measuring $34 \times 34\,\mathrm{mm}^2$. A total of 4 SiPM quads, which comprise of 4 SiPM units. The SiPMs are inserted into designated pin sockets on the front part of the PCB. The functionality of the SiPM is described in Section 3.3.

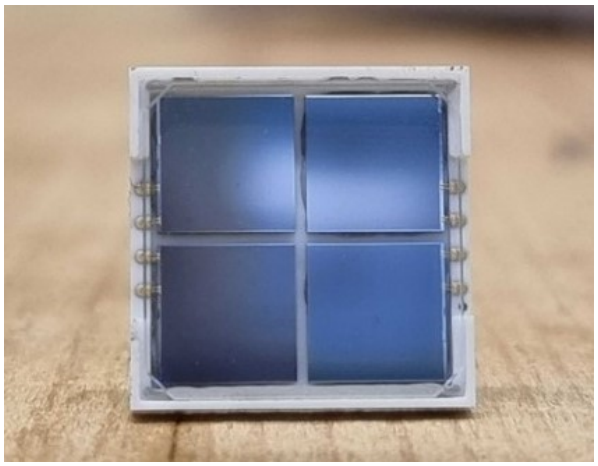

**Figure 10:** A SiPM quad consisting of four individual SiPM units, each measuring 6 x 6 $\mathrm{mm}^2$, which can be mounted on a PCB.

### 4.1.1 Sandbox

Sandbox functions as a dark box maintained at room temperature and is primarily designed to establish a no-light environment. In this experiment, the goal was to assess the functionality of the PCBs.

The PCB was positioned so that the quad was 9 cm from a blue LED. This arrangement was chosen to enable direct illumination of the detector's quadrant by the LED. To ensure

that the measurements could be consistently replicated, a holder was used to securely fix the detector's position and maintain its orientation and stability throughout the testing process, as can be seen in Figure 11. The PCB, and therefore also the quad were powered by 2 power supplies. One was responsible for the signal readout and setting the dynamic range of the pre-amp, wheras the other was powering the SiPM directly, by proving the bias voltage.

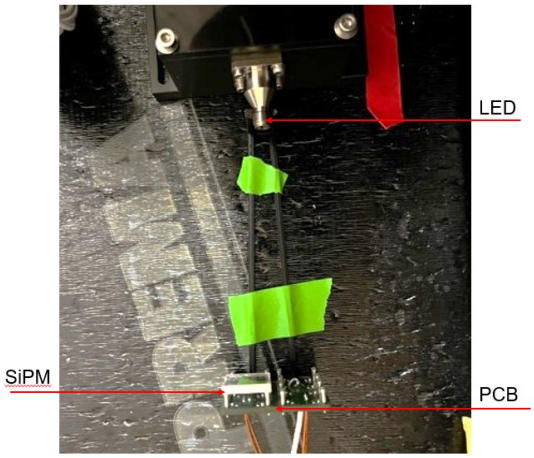


**Figure 11:** The experimental setup in Sandbox, showing the PCB with the mounted quad (bottom) and the LED box (top).

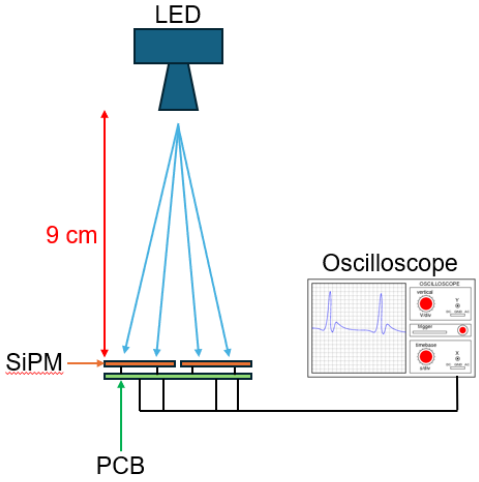


**Figure 12:** Schematic of the experimental setup showing the LED, PCB, SiPM, and oscilloscope.

In the Sandbox experiment, data collection involved an LED configured to emit blue light in square pulses at a frequency of 100 Hz and a pulse width of 50 ns. Three intensities of amplitudes were chosen. Additionally, the bias voltage for the pre-amplifier was incrementally adjusted by 0.5 V. Measurements of peak amplitude in volts over time were recorded using an oscilloscope.

### 4.1.2 LArS

LArS offers a controlled environment in terms of temperature and pressure. It is housed within a dark space that can be filled with a selected gas and making it ideal for SiPM testing [49]. In this case, it was filled with nitrogen to cool the environment surrounding the SiPM and the PCB.

The main component of LArS is a cylindrical vacuum chamber mounted on a frame. The top flange of the vessel is attached to the lower part using screws, and a rubber O-ring ensures a vacuum seal capable of reaching pressures in the order of $10^{-4}$ mbar, via a connected vacuum pump. The inner dimensions of the vessel are 455 mm in height and 250 mm in diameter. The top flange is equipped with several feedthroughs for the vacuum pump connector, gas inlets and outlets, voltage and signal cables, and the cooling system [49].

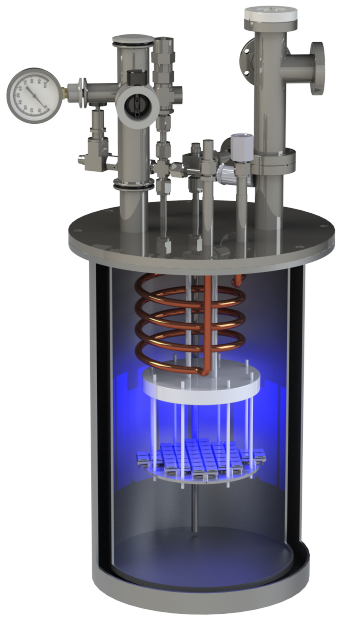

**Figure 13:** Rendered image of the LArS setup, showing the cylindrical vacuum chamber with the cooling system and various feedthroughs.

The cooling system involves an external connector to a tank of liquid nitrogen, which circulates through a copper coil inside the vessel to cool the medium before exiting back to the atmosphere. Temperature control within the cell is managed by adjusting the cold nitrogen flow rate. This adjustment is done through an MKS 0248A-50000RV Flow Control Valve, which is linked to a Cryocon Model 32 Cryogenic Temperature Controller, with readings from two PT100 temperature sensors. [49].

To keep the PCB in place, a holder was designed. The holder used in LArS consists of four main components designed to securely position the PCB inside the vacuum chamber.

There are four slender metal rods extending downwards from the ceiling of the LArS chamber, serving as structural supports for the PCB holder assembly. These rods facilitate height adjustments of the PCB relative to other components such as the cooling system and the LED. There are also four individual clamp components, made out of non-conductive material, which are fixed to the metal rods and securely grasp the PCB edges. The clamp components are linked to the metal rods via adjustable nuts, enabling PCB positioning. The holder features an open and lightweight design to minimize material usage in both clamps and rods. This approach reduces obstruction and ensures effective PCB cooling. The design of the holder can be found in Figure 16.


**Figure 14:** The external setup of LArS showing the cooling system and the vessel.

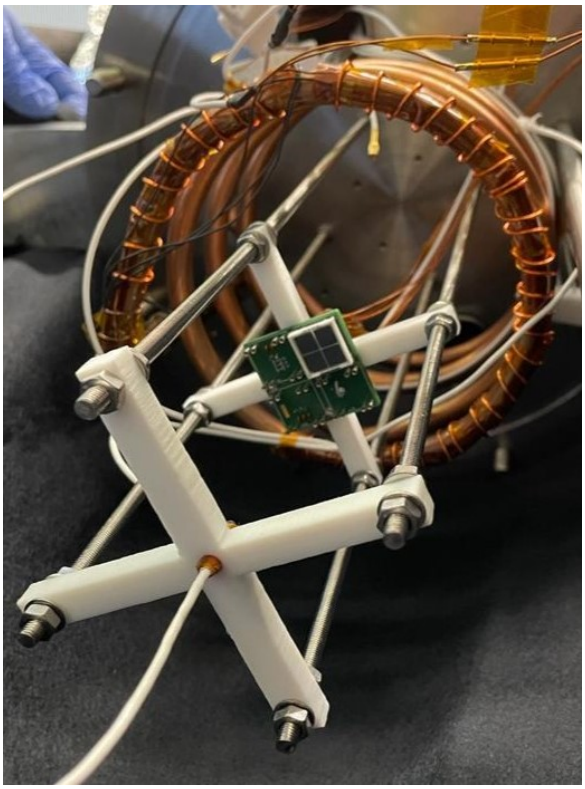

**Figure 15:** The internal view of the LArS vessel showing the PCB holder, the LED, and the SiPM mounted on the PCB.

The positioning of the PCB within the LArS chamber was replicated from the Sandbox configuration to ensure consistency in testing conditions. The quad, mounted on the PCB, was placed 9cm away from the LED.

Figures 17 illustrates the placement of the PCB within the LArS environment. The image shows the underside view of the holder, detailing the arrangement of the supporting rods and clamps, as well as the proximity of the PCB to the cooling coil and LED.

Data collection was done with two main modes. In one mode, blue LED light was directed at the SiPM (LED data). For the other mode, measurements were conducted in a dark setting without any light source (background data). Both setups were restricted to temperatures of 170 K, 190 K, and 210 K.

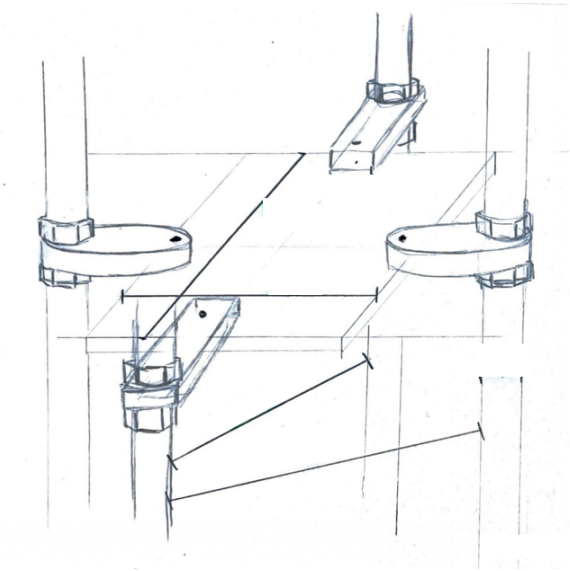

**Figure 16:** PCB holder design.

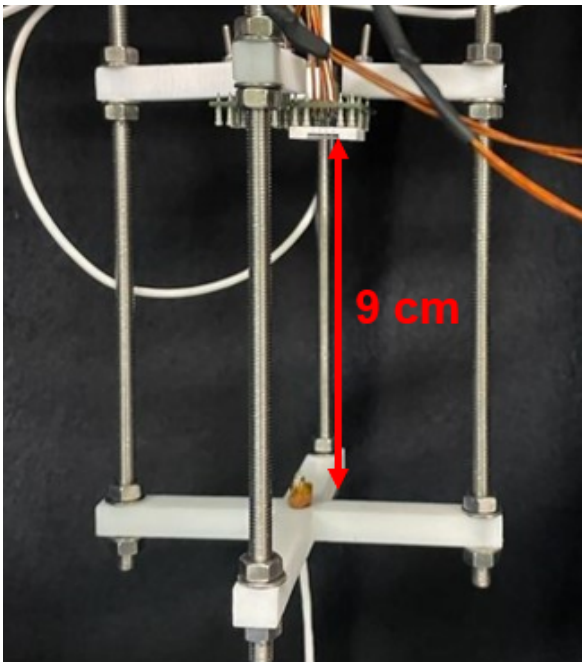


**Figure 17:** Setup of the PCB within the LArS chamber, highlighting the quad's distance from the LED (9 cm) and the cooling system's proximity.

For the LED data, the light source was configured to deliver square pulses at a frequency of 100 Hz and a pulse width of 50 ns. The amplitude of these pulses was varied with temperature to accommodate changes in signal amplitude at different conditions. The bias voltages for the pre-amplifier ranged between 49.5 V and 56.5 V. The data were logged as ADC counts versus time with an ADC. The baseline signal was established by averaging the noise level with the LED off, and was manually set at 14500. This setting corresponds to the 14-bit (16384 range) capacity of the ADC, which is designed primarily for negative signals. Each data-taking mode triggered on the LED signal and recorded 50,000 waveforms.

**Table 1:** Overview of Data Modes and PCB Types

| Data Mode | PCB Type | Environment | Temperatures (K) |
|---|---|---|---|
| LED Data | Original PCB | Illuminated | 170, 190, 210 |
| LED Data | New PCB | Illuminated | 170, 190, 210 |
| LED Data | 16-Channel PCB | Illuminated | 170 to 220 (steps of 10) |
| Background Data | Original PCB | Dark | 170, 190, 210 |
| Background Data | New PCB | Dark | 170, 190, 210 |

In the dark environment only dark counts were expected. For this configuration, triggers were

manually set to detect the peak signals from the dark counts.

All acquired datasets were stored via custom-developed DAQ software as .ROOT files [50].

## 4.2 The PCB and its Properties

This section provides a detailed description of the PCBs utilized during the experiment, including their dimensions, as well as the specifications of the SiPM unit. A total of three different PCBs were tested:

1. The first PCB was previously used in other experiments. It is equipped with an operational amplifier that amplifies voltage and is capable of reading out one signal at a time.
2. The second PCB differs only in the type of operational amplifier used. This amplifier enhances the signal based on a resistance factor and is not dimensionless. A detailed discussion of this PCB is provided in the subsequent sections. Like the first, this board can only read out one signal from the whole board.
3. The third PCB is designed to read out 16 individual signals, one for each SiPM unit. To achieve these readings, it is mounted with micro-coaxial cables. The operational amplifier used in this PCB is the same as that in the second PCB described.

The PCB is used to amplify the signals from the SiPM. A detailed discussion of these operational amplifiers is provided in the Sections 4.2.1, 4.2.2 and 4.2.4

| **Operational Amplifier** | **Signal Readout** | **Cable Type** | **Dynamic Range (V)** |
|---|---|---|---|
| OPA847 | Single Signal | Standard Coaxial | 10 |
| LTC6269-10 | Single Signal | Standard Coaxial | 5 |
| LTC6269-10 | 16 Individual Signals | Micro-Coaxial | 5 |

**Table 2:** Overview of PCB configurations used in the experiment.

### 4.2.1 The Operational-Amplifier AMP-OPA847

The operational amplifier OPA847 is utilized for voltage signal amplification, which supports the reading of individual signals. It provides a 20-fold increase in signal amplitude. The schematic in Figure 18 depicts the circuit configuration for this non-inverting amplifier.

The gain of the amplifier is determined by the feedback resistor $R_{51}$ and the input resistor $R_{48}$. The gain $F_{\text{amp}}$ of the non-inverting amplifier is calculated using the formula:

$$F_{\text{amp}} = 1 + \frac{R_{51}}{R_{48}}, \tag{9}$$

For the given configuration, the calculated gain is:

$$F_{\text{amp}} = 1 + \frac{R_{51}}{R_{48}} = 1 + \frac{2000\Omega}{50\Omega} = 1 + 40, \tag{10}$$

Considering the 50 Ω impedance from the terminations, the actual amplification factor is adjusted by dividing the calculated gain by 2.

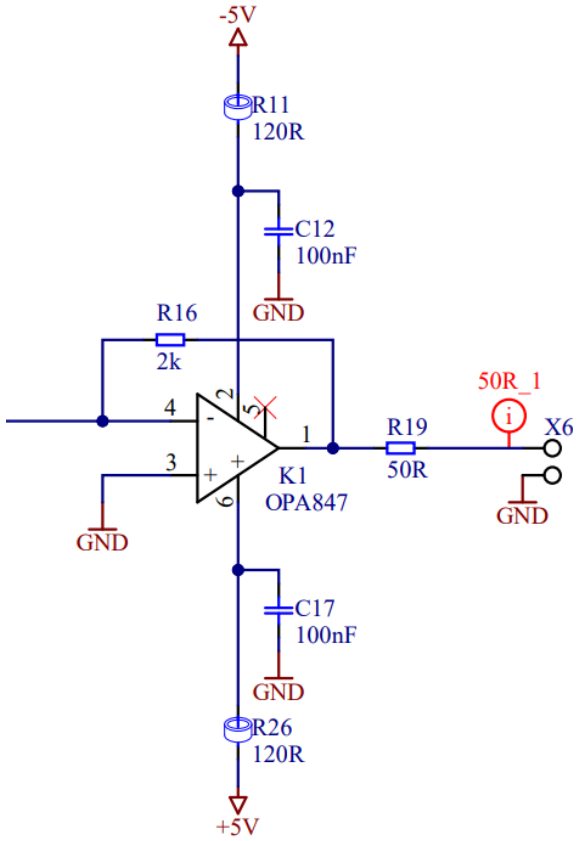


**Figure 18:** Circuit diagram of the operational amplifier OPA847 in a non-inverting configuration.

The PCB on which OPA847 is mounted has nine power wires: three are connected to the pre-amplifier, two serve the SiPMs, and four are allocated for the PT100 temperature sensor. Additionally, there is a singular signal wire for output purposes. The arrangement of these cables is shown in Figure 19. The PCB has a dynamic range of 10 V, which was set by the manufacturer and later tested by the measurements performed in Sandbox, to confirm the value. An op-amps dynamic range refers to the range of input voltages over which the op-amp can operate linearly and provide an accurate output.

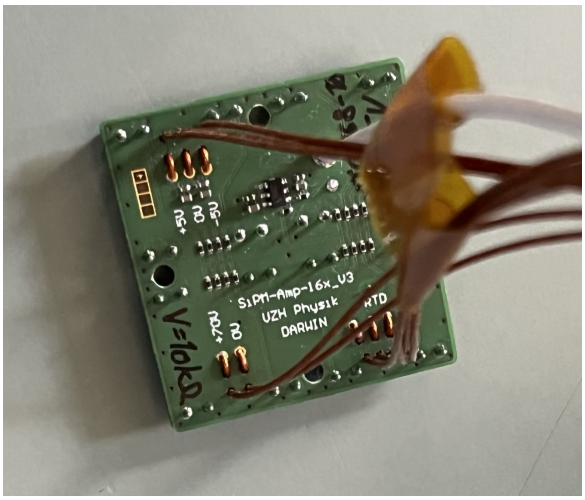


**Figure 19:** Rear view of the PCB showing power cables for the pre-amplifier, SiPMs, and the PT100 temperature sensor, along with the signal cable.

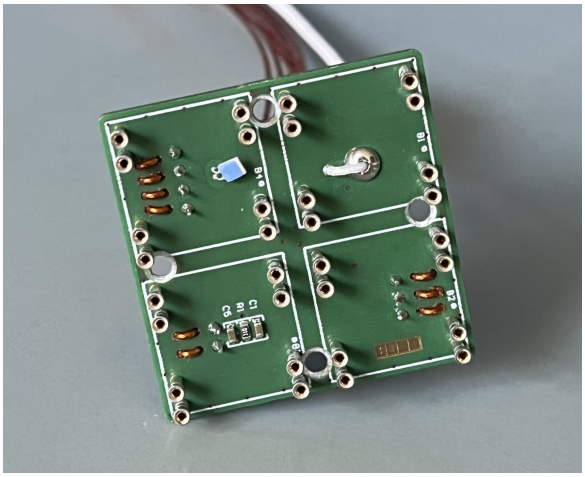

**Figure 20:** Front view of the PCB illustrating the insertion pin sockets for the SiPM quads.

### 4.2.2 The Operational-Amplifier LTC6269-10

The LTC6269-10 operational amplifier offers a different mechanism of action for signal amplification compared to the OPA847. It operates in an inverting configuration where the resistor $R_2$ determines the amplification level. The signal amplification is thus dependent on a resistance factor of 10 kΩ, which contrasts with the previously mentioned dimensionless amplification factor. The output voltage is governed by Ohm's law.

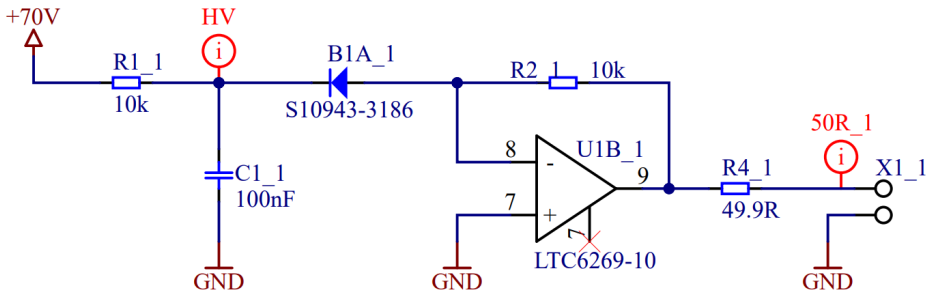


**Figure 21:** Circuit diagram of the operational amplifier LTC6269-10 in an inverting configuration.

The LTC6269-10 operational amplifier is installed on a PCB and was tested for the first time to produce the results shown in this thesis. This op-amp is significant for its ability to have two pre-amplifiers circuits fit into one housing. In scenarios where 16 signals need to be read, such as in this project, this amplifier is ideal because it requires only 8 housing units to be

attached to the PCB instead of 16, which is the case with the OPA847. A much larger PCB would be required to accommodate 16 pre-amp circuits

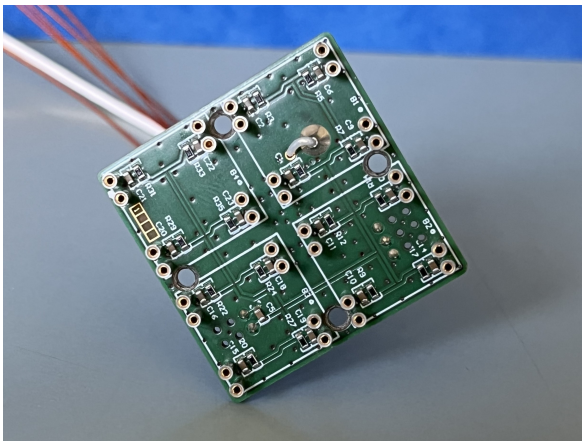

**Figure 22:** Front view of the PCB illustrating the insertion points for SiPMs.

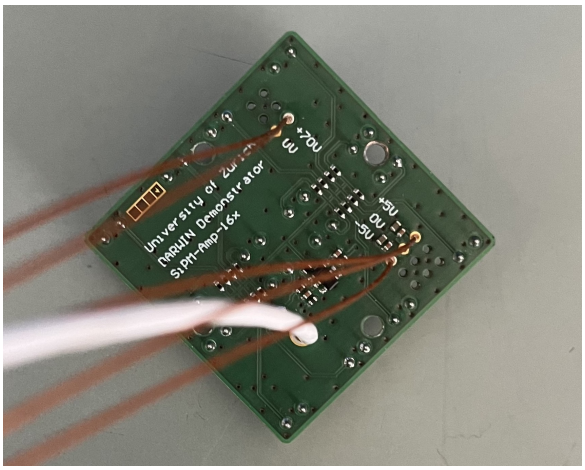


**Figure 23:** Rear view of the PCB showing power cables for the pre-amplifier and SiPMs, along with the signal cable.

The PCB is equipped with five power cables: three for the pre-amplifier and two for the SiPMs. There is also one wire dedicated to signal output, as seen in Figure 23. The PT100 temperature sensor was not included due to space constraints. The PCB has a dynamic range of 5 V, which was set again by the manufacturer and later tested by the measurements performed in Sandbox, to confirm the value.

### 4.2.3 Micro-Coaxial Cables

Micro-coaxial cables function similarly to standard coaxial cables but have a significantly smaller diameter, with the outer diameter being only 0.37 mm compared to 2.03 mm for standard coaxial cables, as can be seen in Table 3. These cables are constructed with a central conducting wire at the core and are enveloped by an insulation layer, a metal shield, and an external layer of insulation. The central conductor, typically made of copper or aluminum, is the pathway for transmitting electrical signals.

Surrounding the central conductor is a dielectric insulator, a non-conductive material that confines the signal to the conductor. This insulation is crucial for maintaining signal integrity, preventing leakage, and protecting against external interferences that could deteriorate the quality of the signal. The performance of the coaxial cable heavily relies on this insulating layer to reduce signal loss.

A metallic shield, made from materials such as aluminum or copper mesh, encircles the insulator. Its main purpose is to prevent interference between the internal signal and electromagnetic disturbances from various sources. This shielding not only protects the signal from external noise but also prevents the signal within the cable from escaping and interfering with adjacent

devices. An outer insulating layer completes the structure of the coaxial cable.

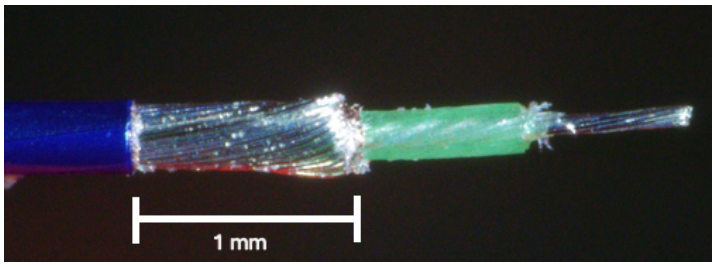


**Figure 24:** Close-up view of a micro-coaxial cable used for signal readout from SiPMs. The components are the central conducting wire, dielectric insulator, metallic shield, and external insulating layer.

The signal from the micro-coaxial cables is converted to standard coaxial cables through a receptacle attached to a middleboard. This receptacle, provided by I-PEX, model Cabline-VS with 20 pins, serves as a interface in this conversion process. The micro-coaxial cables are latched onto this receptacle, ensuring a secure and stable connection that maintains signal integrity. These cables are also soldered to the PCB.

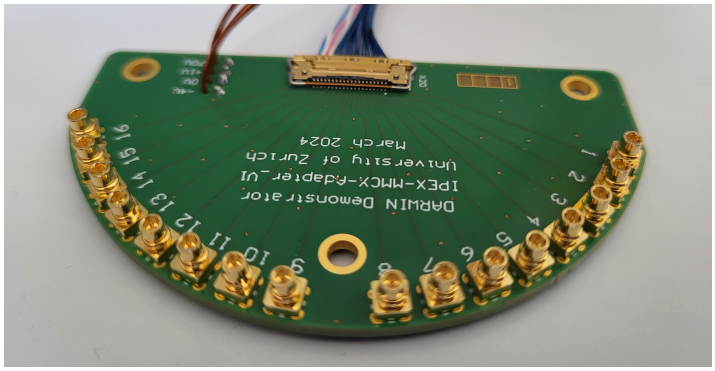


**Figure 25:** Middle board and the I-PEX Cabline-VS receptacle used for converting signals from micro-coaxial cables to standard coaxial cables can be seen at the back of the middle board. This view shows the latching mechanism for the micro-coaxial cables to the middle board.

**Table 3:** Comparison of coaxial and micro-coaxial cable specifications

| Specification | Standard-Coaxial | Micro-Coaxial |
|---|---|---|
| American Wire Gauge | 30 | 40 |
| Inner Diameter (mm) | 0.28 | 0.09 |
| Outer Diameter (mm) | 2.03 | 0.37 |
| Characteristic Impedance (Ω) | 50 | 50 |
| Material of Insulation | PTFE | PFA |
| Vendor | Huber & Suhner | ElectronAix |

Table 3 provides a side-by-side comparison of the specifications for standard coaxial cables and micro-coaxial cables. Both maintain the same impedance of 50 Ohm.

### 4.2.4 16-Channel Readout PCB Design

This sub-section describes the completed 16-channel readout PCB. The board incorporates 8 LTC6269-10 operational amplifiers. Furthermore, the PCB is connected to 16 micro-coaxial cables for signal readout from each SiPM unit. These micro-coaxial cables interface with a middle board serving as an intermediary. The role of the middle board is to transform the signals from the micro-coaxial format to a standard coaxial output, facilitating connectivity with a Data Acquisition (DAQ) system, which first includes the feedthrough and then the digitizer. Figures 26 and 27 depict the PCBs top and bottom side, respectively. The PCB illustrates the layout of the operational amplifiers and the arrangement of the micro-coaxial cables.

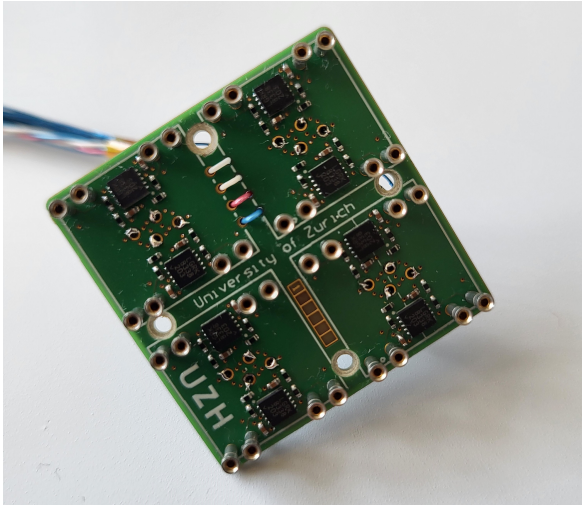


**Figure 26:** Top view of the 16-channel readout PCB, showing the placement of integrated circuits and connections.

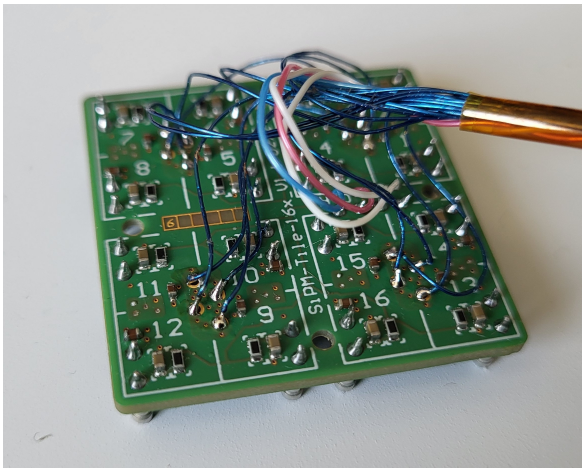

**Figure 27:** Bottom view of the 16-channel readout PCB, illustrating soldered connections and wiring layout.

# 5 Data Analysis and Results

This chapter focuses on the analysis and discussion of the results observed from the collected data. First, it covers the results from Sandbox, which provides a foundation for further analysis of the data from LArS. The LArS measurements, having a more complex system and analysis, include a detailed explanation of the methodological approach.

## 5.1 Sandbox measurements

As described in Section 4.1.1, the acquisition of only LED ON data in the Sandbox environment was done using an oscilloscope focusing on the waveform shapes and associated noise levels. In particular, the oscilloscope recorded the mean amplitude and the amplitude's standard deviation. The following subsection will highlight the PCBs performances at room temperature.

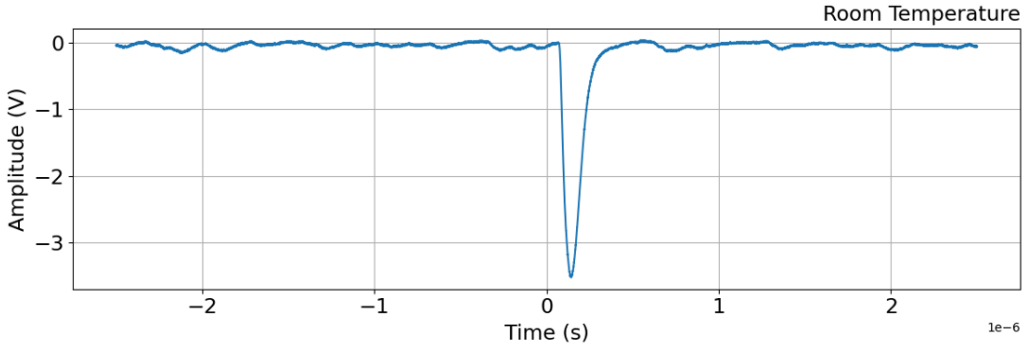


**Figure 28:** Waveform acquired with the new PCB recorded at room temperature with an oscilloscope.

The oscilloscope recording depicted in Figure 28 reveals distinct characteristics of the waveforms generated by the new PCB. The waveform exhibit a sharp rise time of approximately 90 ns at room temperature. Notably, the decay time of approximately 270 ns surpasses the rise time, as illustrated in the figure. The original PCB, in comparison, has a faster rise time of about 30 ns, attributed to the amplification factor of 20 coming from the pre-amplifier.

These measurements aimed to evaluate and compare the performance of the two PCBs: one equipped with LTC6269-10 operational amplifier and another with the previously tested AMP-OPA847 op-amp. The comparison centered on the mean amplitude under three different light intensities corresponding to setting the voltage provided to the LED to 3.130 V (low), 3.230 V (medium), and 3.330 V (high). The bias voltage was adjusted in increments of 0.5 V within a range from 53.5 V to 57.5 V. The power supply for the pre-amplifier of the original PCB was set between -5 V to 5 V, while for the pre-amplifier of the new PCB it was limited to -2.5 V to 2.5 V, because of its narrower dynamic range. Figure 29 depicts the differences between the data from the two PCBs.

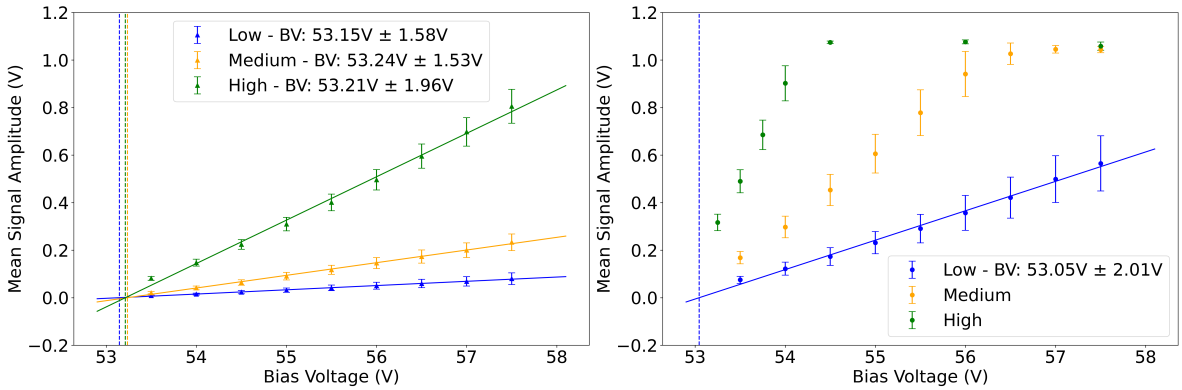


**Figure 29:** Comparative analysis of the mean signal amplitude for both PCB configurations under different bias voltages, showing the mean amplitude of the signals. Each PCB was tested under three LED intensities common to both PCBs. The dynamic range is set to -5 V to 5 V for the original PCB with the AMP-OPA847 op-amp, and -2.5 V to 2.5 V for the new PCB with the LTC6269-10 operational amplifier. The dashed lines represent the breakdown voltage of the SiPM, which are extrapolated by making a linear fit for the data and taking their roots.

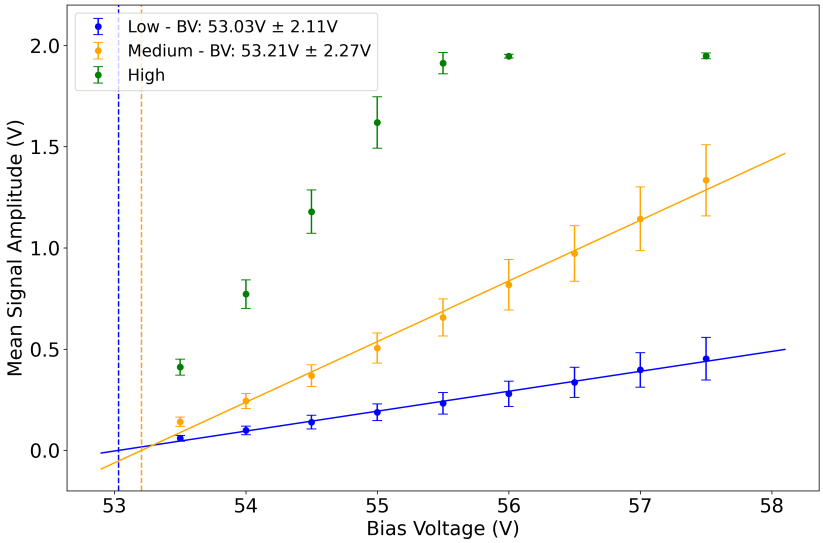


**Figure 30:** Analysis of the mean signal amplitude for the new PCB configuration under different dynamic ranges and bias voltages. The figure shows the mean amplitude of the signals under three different LED intensities. The dynamic range is set to -4.5 V to 0.5 V for the modified setting of the new PCB with the LTC6269-10 operational amplifier. The dashed lines represent the breakdown voltage of the SiPM, which are extrapolated by making a linear fit for the data and taking their roots.

Figure 29 shows that the original PCB detects signals with less variance in amplitude for the

same light intensity compared to the new PCB. The signal amplitudes of the new PCB begin to saturate at mid and high intensities due to a dynamic range limited to -2.5 V to 2.5 V. To optimize signal detection and reduce saturation effects, the new PCB was tested with a modified dynamic range of -4.5 V to 0.5 V. Such change is possible because the signal from the SiPM are asymmetric and always negative. Figure 30 presents a comparison of amplitude signals between the two PCBs with the different ranges.

By the dynamic range to -4.5 V to 0.5 V, the detectable signal amplitude was increased without loss of signal quality, and the waveforms remained stable, and free from ringing. Given the clear improvement all subsequent results were obtained by operating the new PCB with the same dynamic range. Further analysis was carried out in LArS to examine the implications of the large variances on other extracted parameters.

## 5.2 LArS measurements

As previously explained, measurements in LArS were conducted at temperatures set at 170 K, 190 K, and 210 K, which allowed for a more intricate analysis. The data were saved as ROOT files on a computer using custom-built DAQ software. Therefore, before initiating the data analysis, the files needed to undergo preprocessing.

### 5.2.1 Processing of Files

The data files contain a total of 10'000 recorded waveforms for LED ON operation and 50'000 waveforms for LED OFF data taking periods. The processing of the raw data files is identical for both LED ON and LED OFF runs. This processing involves determining peaks in the waveform and distinguishing them from noise fluctuations. The baseline is calculated by taking the median of the first 50 samples of the waveform. One sample corresponds to 10 ns. If a dark count occurs within these first 50 entries, the baseline may be slightly affected; this is, however, a small effect when blended into all 50 entries. Additionally, the root mean square (RMS) is calculated from these waveforms. An event is considered a signal once it exceeds 5 RMS, as depicted in Figure 31.

The data processing creates a dataframe that includes all identified peaks from a SiPM readout. Each entry contains key parameters: waveform number, peak sequence number (if multiple peaks are detected), signal duration, peak position, and signal area. The peak position is defined as the first waveform sample exceeding five times the root-mean-square (RMS) deviation from the baseline and indicates when the peak starts in relation to the waveforms beginning. The signal area, measured in integrated ADC counts, represents the total charge collected during the peak.

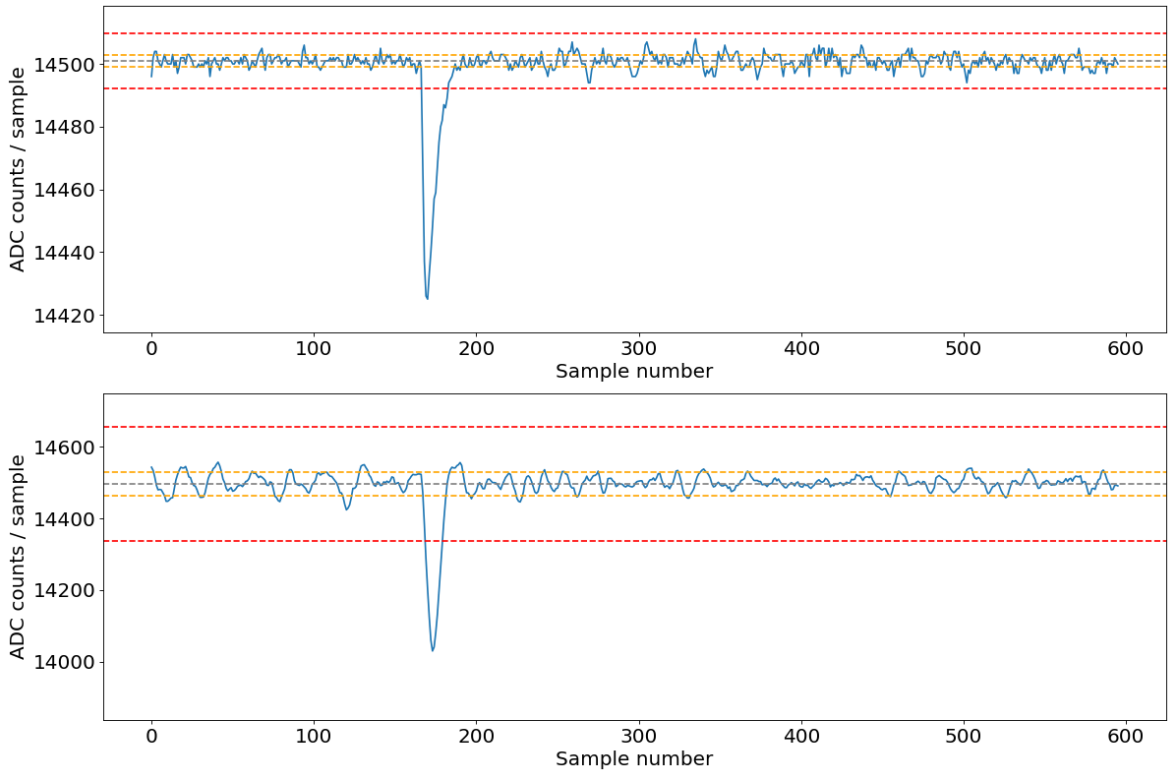


**Figure 31:** Comparison of waveforms of a single photoelectron event obtained with the original PCB (top) with that of the new PCB (bottom) under no illumination. Waveforms were taken at 170 K with a bias voltage input of 54.5 V. The yellow dashed lines represent one standard deviation from the baseline, while the red dashed lines indicate 5 RMS, the threshold for signal detection.

When comparing the waveforms in Figure 31, it is evident that the signal from the new PCB is notably larger than that from the original one, when comparing the y-axis to each other. This disparity can be attributed to the higher amplification of the signal by the op-amp used in the new PCB compared to the old one. Consequently, the noise is also amplified to a greater extent, resulting in larger fluctuations. These fluctuations impact the root mean square (RMS), as can be observed in the figure.

### 5.2.2 Background Data: DCR and CTP

In the absence of LED illumination, the signals read out with the SiPMs correspond only to dark counts and noise. Figure 32 displays an area histogram without any cuts applied. The spectra shown corresponds to two different PCB settings at 170 K under a bias voltage of 54.5 V. In the histogram for the original PCB (top), the noise manifests as a peak near an area of zero, followed by the 1 PE and 2 PE peaks at approximate areas of 6,000 and 13,000 integrated ADC counts respectively. For the new PCB (bottom), the 1 PE and 2 PE peaks appear at around 30,000 and 70,000 integrated ADC counts respectively. Each of these peaks

is succeeded by a "shoulder" of signals, the origins of which are not well-defined but have been documented in studies of the same SiPM model [51]. Signals exceeding half the median area of the 1 PE peak are categorized as dark counts rather than noise, denoted as the 0.5 PE area.

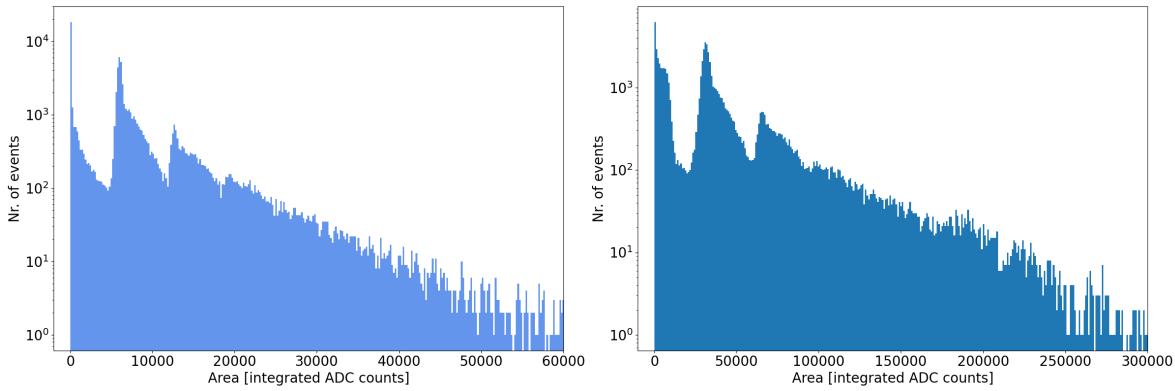


**Figure 32:** Histograms of signal areas with no cuts applied, taken at 170 K under a bias voltage of 54.5 V, showing the distribution of dark counts and noise. The upper histogram corresponds to the original PCB equipped with the AMP-OPA847 op-amp, and the lower histogram corresponds to the new PCB equipped with the LTC6269-10 operational amplifier. The noise manifests as a peak near zero area, followed by the median areas of the 1 PE and 2 PE peaks.

Figure 32 demonstrates that the outputs from the two PCBs under identical conditions are fairly consistent. The notable exception is that the area from the new PCB is increased because of greater amplification by 10 Ω from the operational amplifier, as expected.

To accurately identify the 1 PE peak, appropriate cuts in signal length and position of the identified peaks have been applied. The goal is to filter out the noise contribution that occurs before the single photoelectron peak, while maintaining the latter.

Figure 33 displays the SPE spectrum under various cuts. The blue histogram represents the entire spectrum without any applied cuts. The orange histogram includes only position cuts, which are uniformly set at 150 and 190 for both PCB configurations, aiming to reduce the background noise. The green histogram illustrates the spectrum after applying both position and length cuts to reduce the noise even further. This approach enables precise isolation of the SPE peaks and enhances the comparability of data from the original and new PCBs.

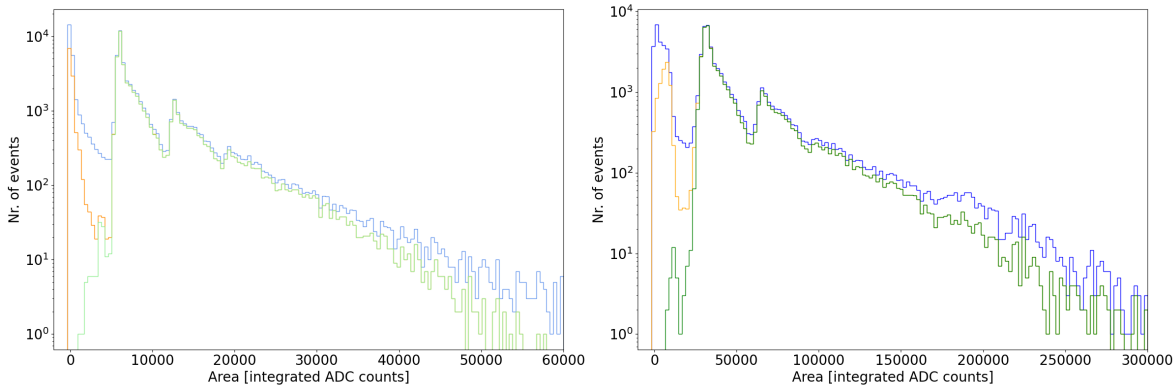


**Figure 33:** Comparison of the SPE peak region with different cuts applied, using data taken at 170 K. The blue histogram shows the complete spectrum without any cuts. The orange histogram includes only position cuts (150 to 190 samples) to reduce the background. The green histogram applies both position (150 to 190 samples) and signal length cuts, specifically at 10 samples for the original PCB and at 9 samples for the new PCB, to isolate the Gaussian peak of the SPE. The upper histogram displays data from the original PCB with the AMP-OPA847 op-amp, while the lower one is from the new PCB with the LTC6269-10 operational amplifier.

The specific length cuts applied are as follows:

- **Original PCB:**
  - At 170 K: lower cut at 10 samples
  - At 190 K: lower cut at 8 samples
  - At 210 K: lower cut at 8 samples
- **New PCB:**
  - At 170 K: lower cut at 9 samples
  - At 190 K: lower cut at 5 samples
  - At 210 K: lower cut at 3 samples

For the analysis of the dark count rate the SPE peak is fitted with a Gaussian function, from which the mean, $\mu$, and standard deviation, $\sigma$, can be extracted. Calculating the integral of the area histogram over multiple starting points and performing a subsequent differentiation, a distinct peak in the derivative was found at the 1 PE position, as depicted in Figure 34.

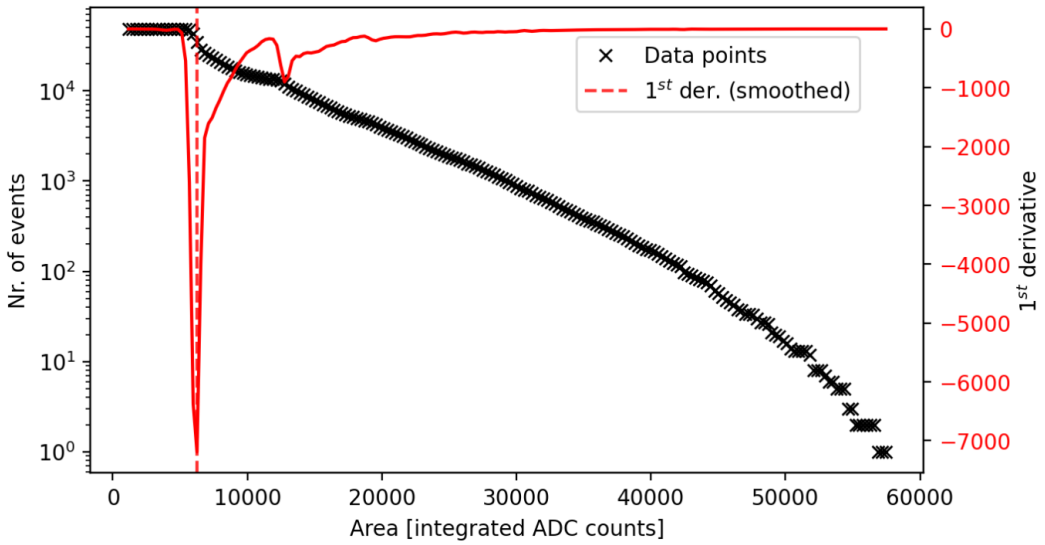


**Figure 34:** Differential analysis of the area histogram to identify the 1 PE peak. Area histogram obtained with the original PCB at 170 K for a bias voltage of 54.5 V. The peak median, $\mu$, illustrated as the dotted line, represents the location of the 1 PE peak.

The prominent peak depicted in Figure 35 provides a basis for precise SPE peak identification. A Gaussian fit, initiated with the mean at the minimum point of the derivative (marked by the dotted line in Figure 35) aids in the computation of the DCR. The peak's mean value, $\mu$, is used to denote the position of the 1 PE peak, as shown in Figure 35.

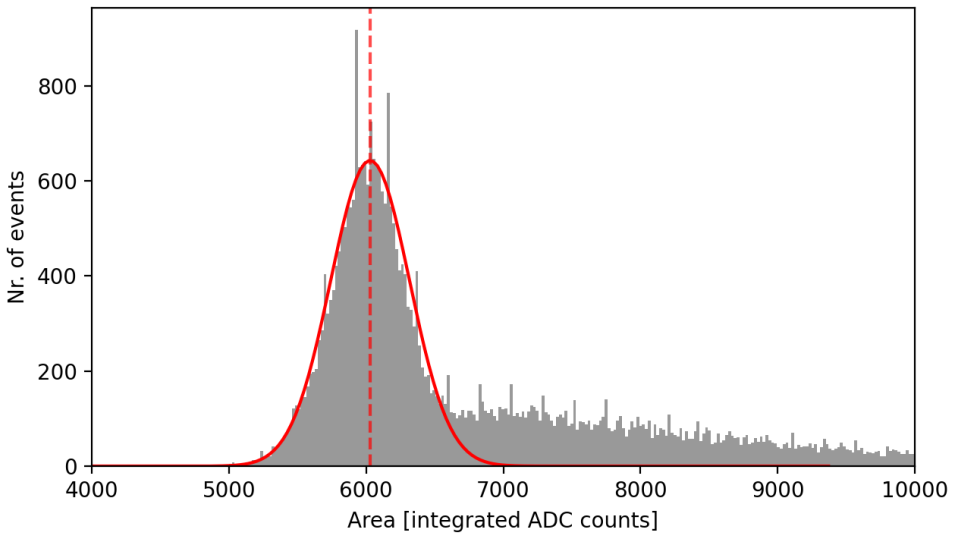


**Figure 35:** Identification of the SPE peak with a Gaussian fit. The dotted line indicates the minimum of the derivative, centering the Gaussian fit.

Following the successful fit of the SPE peak, the 0.5 PE threshold is derived by taking $\mu/2$. This threshold designates the signals that are considered dark counts. To effectively calculate the DCR, equation (11) is used:

$$DCR = \frac{N_{0.5}}{A_{\text{SiPM}} \cdot t}, \tag{11}$$

Where $A_{\text{SiPM}}$, equal to 144 $\text{mm}^2$, reflects the combined area of a quad consisting of four SiPM units, each measuring $6 \times 6\,\text{mm}^2$. The DCR is then found by normalizing the frequency of signals surpassing the 0.5 PE threshold, $N_{0.5}$, against this SiPM area and the measurement time, $t$. This calculation is applied to data sets acquired at temperatures of 170 K, 190 K, and 210 K, and bias voltages between 49.5 V and 56.5 V. The DCR error is estimated using equation (12):

$$\sigma_{DCR} = \frac{\sqrt{N_{0.5}}}{A_{\text{SiPM}} \cdot t}, \tag{12}$$

Figure 36 shows the DCR values for both the original and new PCB. The graphs suggest a proportional increase in DCR with higher overvoltage inversely correlated with the decrease in temperature. Overvoltage is defined as the magnitude of voltage exceeding the breakdown voltage threshold of the SiPM. Detailed calculations of this breakdown voltage are provided in Section 5.2.3. Notably, at 210 K, deviations from the linear trend are observed, particularly with the original PCB. This anomaly is attributed to inaccuracies in the measurement time caused by the DAQ system entering a 'busy mode', which occurs when the system is saturated with signals, exceeding its processing capacity, resulting in an extended measurement duration.

Figure 37 shows the differences in performance between the original and new PCB at 170K. At this temperature, both PCB configurations exhibit significantly lower DCR values across the entire range of bias voltage settings compared to those observed at higher temperatures, averaging at about 1 dark count per second.

As explained in Subsection 3.3.1, crosstalk in a pixel array is a process in which an excited electron in one pixel generates a photon that triggers an additional avalanche in an adjacent pixel. The CTP measures the frequency of such events relative to the detected dark counts. The equation to calculate the effective DCR is shown in equation (13):

$$CTP = \frac{N_{1.5}}{N_{0.5}}, \tag{13}$$

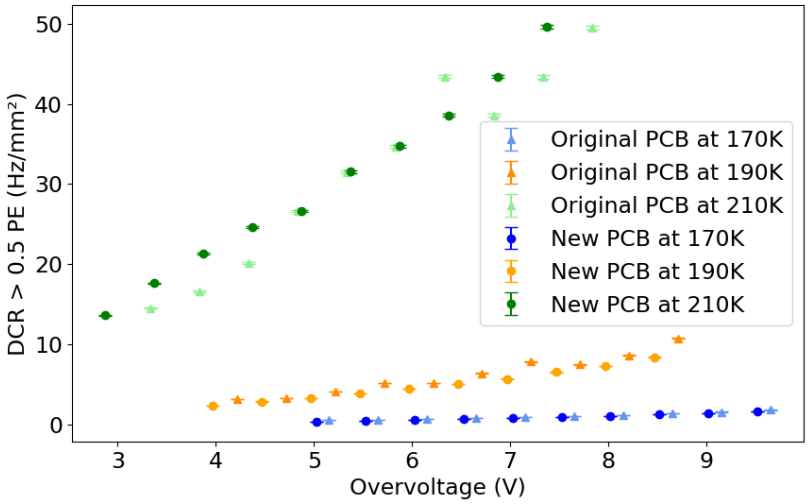


**Figure 36:** Comparison of DCR versus overvoltage for the original and new PCBs at different temperatures. The trend indicates a linear DCR increase with overvoltage, with deviations at 210 K for the original PCB due to the DAQ busy mode affecting the measurement time.

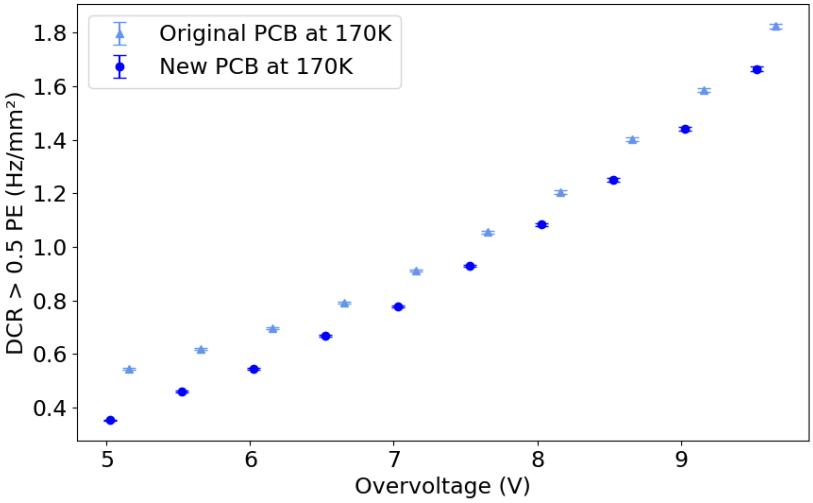


**Figure 37:** Comparison of DCR versus overvoltage for the original and new PCBs specifically at 170K. This temperature regime shows notably lower DCR values.

Where $N_{1.5}$ is the number of crosstalk events, here defined as events beyond the 1.5 PE threshold, and $N_{0.5}$ is the total number of dark counts, characterized as events beyond the 0.5 PE threshold, as mentioned above. The error on the CTP is calculated by error propagation as shown in equation (14):

$$\sigma_{CTP} = CTP \cdot \sqrt{\left(\frac{\sigma_{N_{1.5}}}{N_{1.5}}\right)^2 + \left(\frac{\sigma_{N_{0.5}}}{N_{0.5}}\right)^2}. \tag{14}$$

Figure 38 shows the CTP as a function of overvoltage for the recorded temperatures. The graph illustrates the data for the original and the new PCB. The crosstalk probability exhibits a proportional relationship with the overvoltage. At lower gains, the CTP tends towards zero.

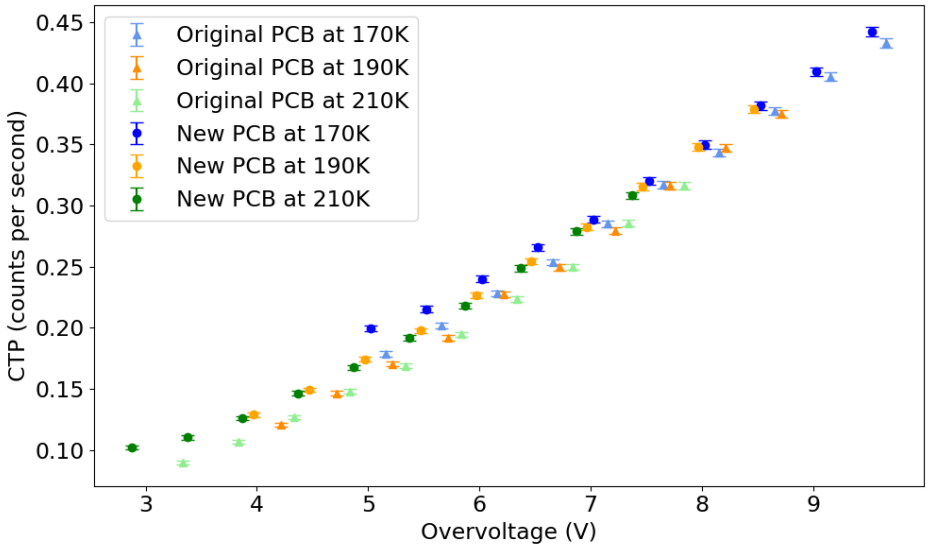


**Figure 38:** CTP as a function of overvoltage for both original and new PCBs at various temperatures. The trend shows a proportional increase in CTP with overvoltage, with CTP nearing a lower limit at reduced gains.

### 5.2.3 Background Data: Gain and Breakdown Voltage

To initiate the subsequent analysis, it was important to extrapolate the breakdown voltage of the SiPM at the tested temperatures (170 K, 190 K, and 210 K). This was accomplished by determining its gain at each temperature. Although the gain for both PCBs was expected to be the same, their calculations differ because each PCB utilizes a different operational amplifier.

For the general calculation of the gain, it is important to know that the intensity of a signal is dictated by the quantity of photons reaching the SiPM; specifically, by the number of APD activated within the SiPM and the voltage of operation. When the SiPM operates without illumination, the peaks from the activated APDs become visible, identified as 1 PE for one activated APD, 2 PE for two activated APDs, etc. The gain is then calculated as the ratio of the final charge to the initial charge as in equation (15):

$$G = \frac{Q}{q_e}, \tag{15}$$

where $q_e$ is the elementary charge. The formulation of $Q$ varies between the two PCBs due to differing op-amps. For the original PCB, $Q$ is expressed as stated in equation (16):

$$Q = \int I\,dt = \frac{1}{R} \cdot F_{\text{amp}} \int V\,dt = \frac{\text{ADC}_{\text{range}}}{R \cdot F_{\text{amp}} \cdot \text{ADC}_{\text{res}}} \int \text{ADC}_{\text{counts}}\,dt, \tag{16}$$

where $Q$ represents the total charge from all avalanches in the SiPM. $R$, the impedance of the ADC, is $50\,\Omega$. The total amplification factor, $F_{\text{amp}}$, is 20 for the original op-amp, as calculated in Section 4.2.1. $\text{ADC}_{\text{res}}$ is the resolution of the ADC at 14 bits, or 16384 levels. $\text{ADC}_{\text{range}}$ is the ADC's total voltage range, set at 2.25 V. $\text{ADC}_{\text{counts}}$ represents the mean area for a single photoelectron (SPE) peak. This definition of gain corresponds to the number of electrons released per avalanche triggered by a single photon impact on the SiPM.

For the new PCB, $Q$ is formulated as stated in equation (17):

$$Q = \int I\,dt = \frac{1}{R} \int V\,dt = \frac{\text{ADC}_{\text{range}}}{R \cdot \text{ADC}_{\text{res}}} \int \text{ADC}_{\text{counts}}\,dt, \tag{17}$$

Where $F_{\text{amp}}$ is omitted because the op-amp LTC6269-10 includes amplification within its resistance specification.

The gain was computed and its relationship with the bias voltage was graphically represented to determine the breakdown voltage. This was achieved by applying a linear fit to the gain versus bias voltage data and extrapolating to find the intersection with the voltage axis, which provides the breakdown voltage, as shown in Figure 39.

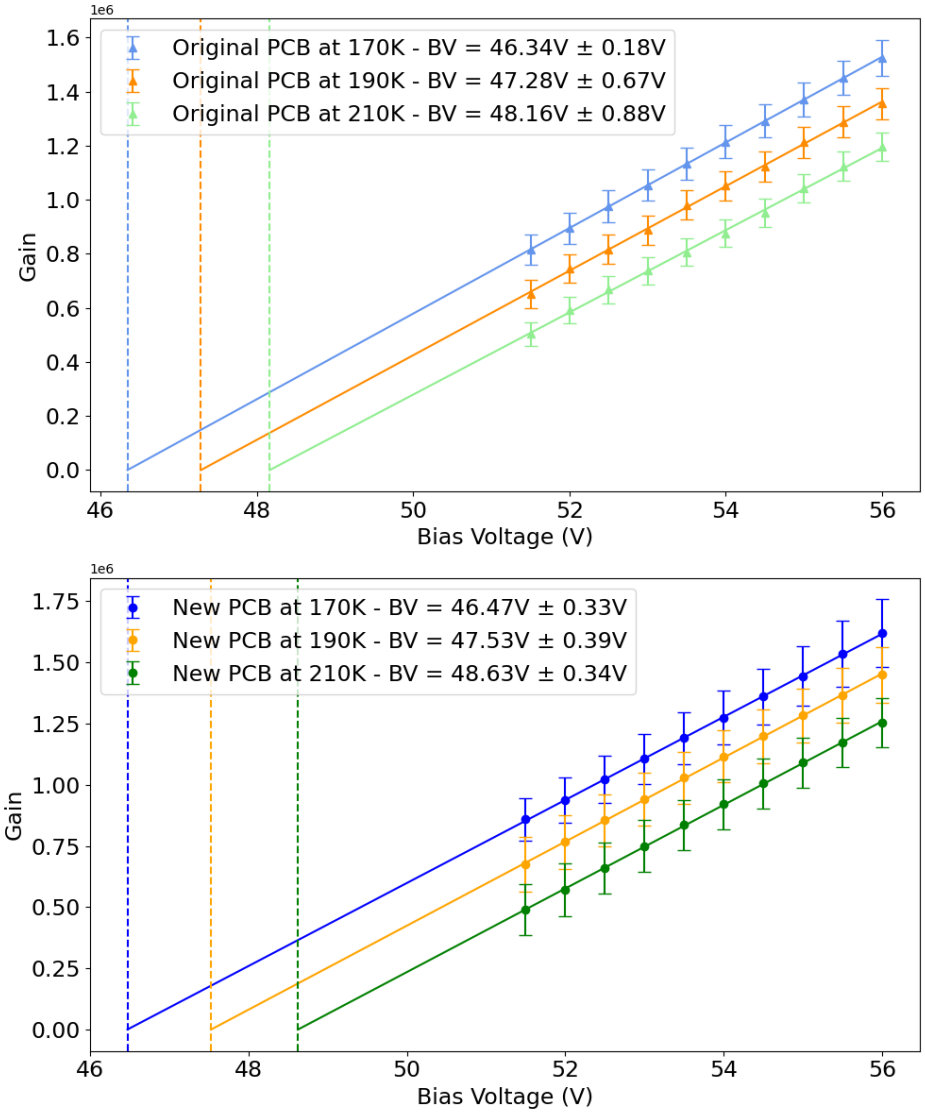


**Figure 39:** Linear fit of gain against bias voltage to extrapolate the breakdown voltage for both original (upper) and new (lower) PCB at different temperatures.

For each temperature, uncertainties in the breakdown voltage (BV) were derived from the slope and intercept standard errors of the gain versus voltage linear regression. A direct linear relationship between gain and bias voltage is observable in Figure 39 alongside a reduction in gain corresponding to rising temperatures. This is observed for both PCBs. This reduction can be attributed to the increase in breakdown voltage at higher temperatures. Consequently, the overvoltage at which the SiPM operates is lower at elevated temperatures compared to lower temperatures. However, when examining gains plotted against overvoltage as shown in Figure 40, it becomes evident that the gains are consistent across different temperatures, indicating a lack of temperature dependence on the gain when normalized to

overvoltage.

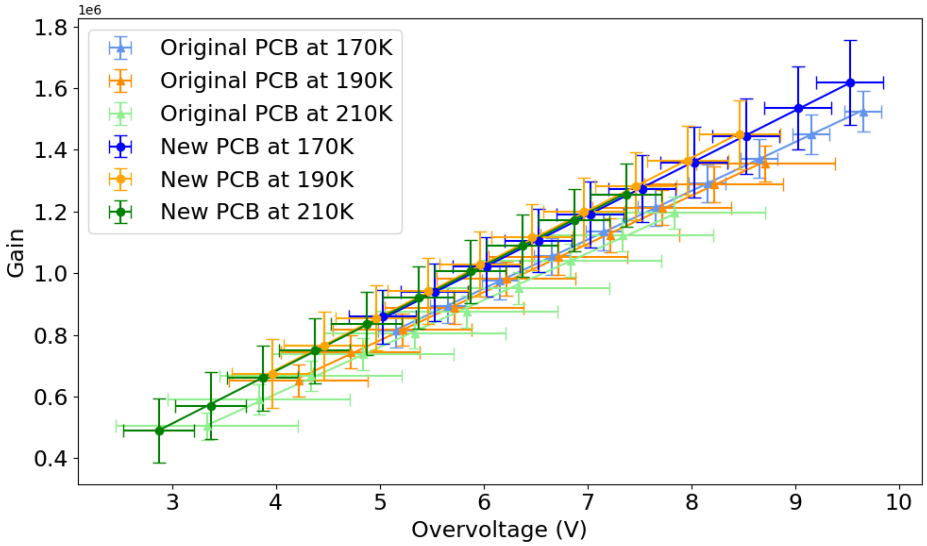


**Figure 40:** Gain as a function of overvoltage for both the original and new PCBs at different temperatures.

On the other hand, Figure 40 shows the gain plotted against the overvoltage, revealing minimal temperature influence for both PCBs, as expected. There a difference of about 10% in gain when comparing the original to the new PCB. This can be attributed to the error on the calculation of the breakdown voltage.

### 5.2.4 Background Data: SPE Resolution

The calculation of the SPE resolution employs the values of $\mu$ and $\sigma$ derived from the fit to the SPE peak, as employed in the DCR analysis. SPE resolution quantifies the SiPM's precision in identifying photon-induced signals. This resolution is given by the ratio of $\sigma$ to $\mu$, as defined in equation (18):

$$\mathrm{SPE}_{\mathrm{res}} = \frac{\sigma}{\mu}. \tag{18}$$

In Figure 41, the SPE resolution of both PCBs is plotted against the gain.

Noteworthy is the fact that the original PCB has a better SPE resolution than the new PCB. This is likely be due to the stronger amplification on the latter. This also reflects in the higher variance, already seen in the Sandbox test. Also temperature fluctuations within LArS can result in a shift of the results. The original PCB has a relative resolution of about 4 to 8%, whereas the value for the new PCB varies from 8 to 22%, depending on the temperature and bias voltage applied. The SPE resolution is highest for high gain and low temperatures. A difference of 4% can be observed between the two PCBs for a high gain.

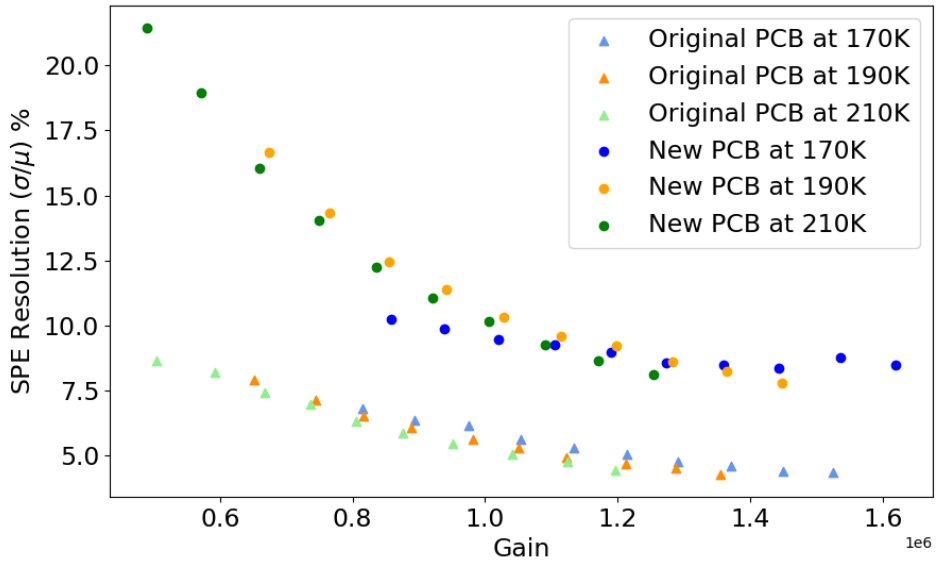


**Figure 41:** SPE resolution plotted as a function of gain for both the original and new PCBs.

### 5.2.5 LED Data: Comparison of Signals

The PCBs were tested under illuminated conditions at temperatures of 170 K, 190 K, and 210 K, with LED intensity levels of high, medium, and low. These tests aimed to compare signal characteristics under illumination. The results of these tests are summarized in Table 4, which shows the LED signal voltages corresponding to different LED intensities at the specified temperatures.

| Temperature (K) | Low Intensity (V) | Medium Intensity (V) | High Intensity (V) |
|---|---|---|---|
| 170 | 3.10 | 3.15 | 3.20 |
| 190 | 2.75 | 2.78 | 2.80 |
| 210 | 2.61 | 2.64 | 2.67 |

**Table 4:** Comparison of LED signal voltages at various temperatures and intensities.

A comparison of a single waveform from both PCBs tested under identical conditions at 170 K, with a 54.5 V bias voltage, and an LED signal voltage of 3.15 V is shown in Figure 42. The top plot illustrates the response from the original PCB, whereas the bottom plot displays the output from the new PCB. The new PCB demonstrates a higher signal amplification compared to the original, in addition to exhibiting a notable overshoot following the signal's decline. Despite this, the overshoot does not impact the data analysis, because its not identified as the primary signal.

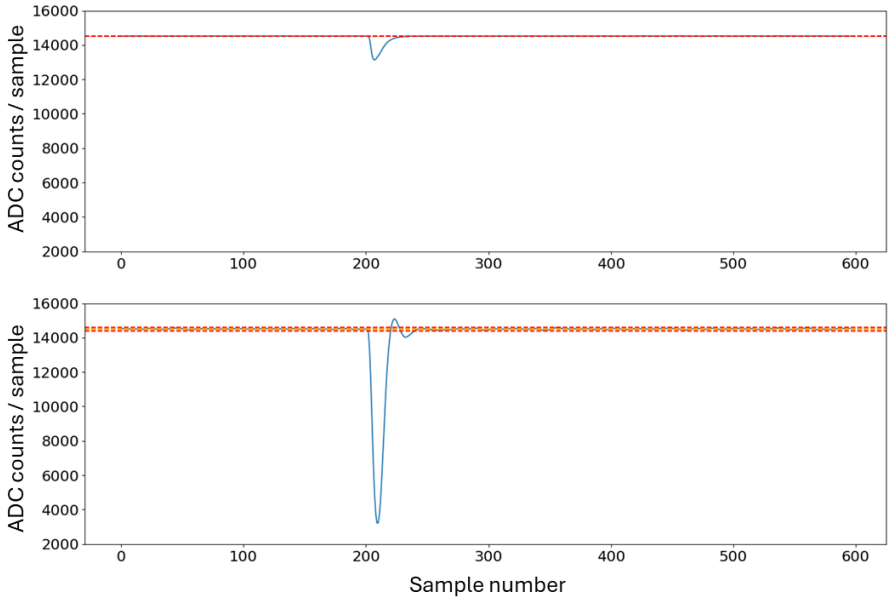


**Figure 42:** Comparison of waveform responses under identical testing conditions at 170 K, 54.5 V bias voltage, and 3.15 V LED signal voltage. The top plot represents a single waveform from the original PCB, and the bottom plot from the new PCB.

Figure 43 depicts the signal area of the original and new PCB at 170 K to LED pulses. The LED was set to an amplitude of 3.15 V amplitude, a 50 ns pulse width, and a 100 Hz frequency. Bias voltages were set within a range of 51 V to 55 V. The signal area gets smaller as the bias voltage is lowered, following the reduction of the gain with over-voltage; a trend also observed in both PCBs.

For effective signal comparison, normalization was performed by dividing the signal area by the median peak value from the original and the new PCB (at a 170 K temperature setting with a 54.5 V bias voltage and a 3.15 V LED amplitude). Overlaid histograms from the original and new PCBs can be seen in Figure 44.

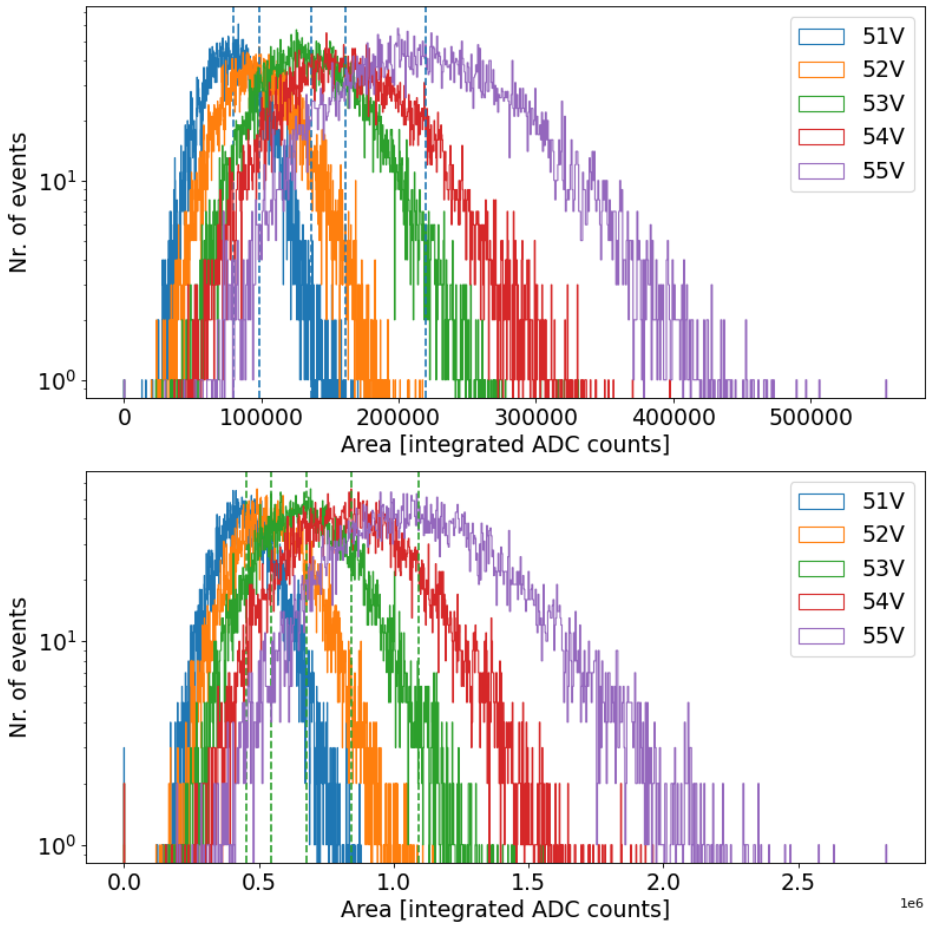


**Figure 43:** Comparison of signal areas from LED pulses at 170 K for the original and new PCBs. Both setups utilized an LED with a medium amplitude intensity of 3.15 V, a pulse width of 50 ns, and a frequency of 100 Hz, across bias voltages ranging from 51 V to 55 V. The yellow dashed lines represent one standard deviation from the baseline, while the red dashed lines indicate 5 RMS, the threshold for signal detection.

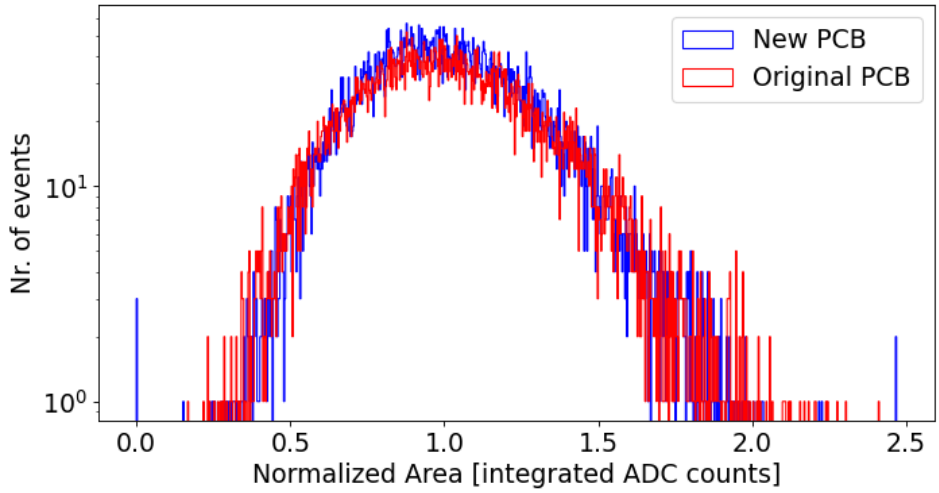


**Figure 44:** Normalized signal areas from the original and new PCB at 170 K, with a 54.5 V bias voltage and a medium LED amplitude intensity of 3.15 V.

The signals show little variation between them. This supports the conclusion that the stronger amplification by the new PCB's op-amp does not fundamentally change the signal shape. Consequently, parameters such as DCR, CTP, and gain, which are derived from these signals, remain unaffected by the increased amplification provided by the new PCB's operational amplifier.

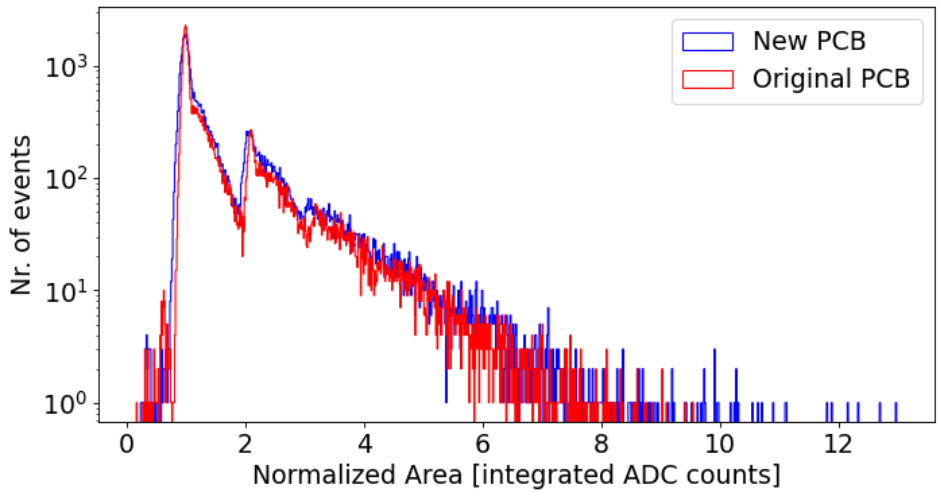


**Figure 45:** Normalized background signal comparison from the original and new PCB at 170 K, under no LED conditions with a bias voltage of 54.5 V.

When comparing signals in the absence of illumination, as illustrated in Figure 45, signals from both PCBs are comparable. As expected for high gains, as in this case where the bias

voltage was set to 54.5 V, the difference in SPE resolution observed in Section 5.2.4 of about 2%, is not observable in the normalized area spectra.

### 5.2.6 First tests using the 16-channel readout PCB

This section outlines the preliminary analysis of data taken with the 16-channel readout PCB. Because of the availability of a single SiPM quad, the analysis was limited to four channels. The analysis of the PCB remains the same as for the prior PCBs, the only difference now being the readout of 4 signals simultaneously. As a starting condition, the PCB was tested at room temperature in LArS with a bias voltage set to 56 V and the LED amplitude set to 2.4 V, in square pulses at a frequency of 100 Hz and a pulse width of 50 ns. Figure 46 illustrates the 4 signals at room temperature.

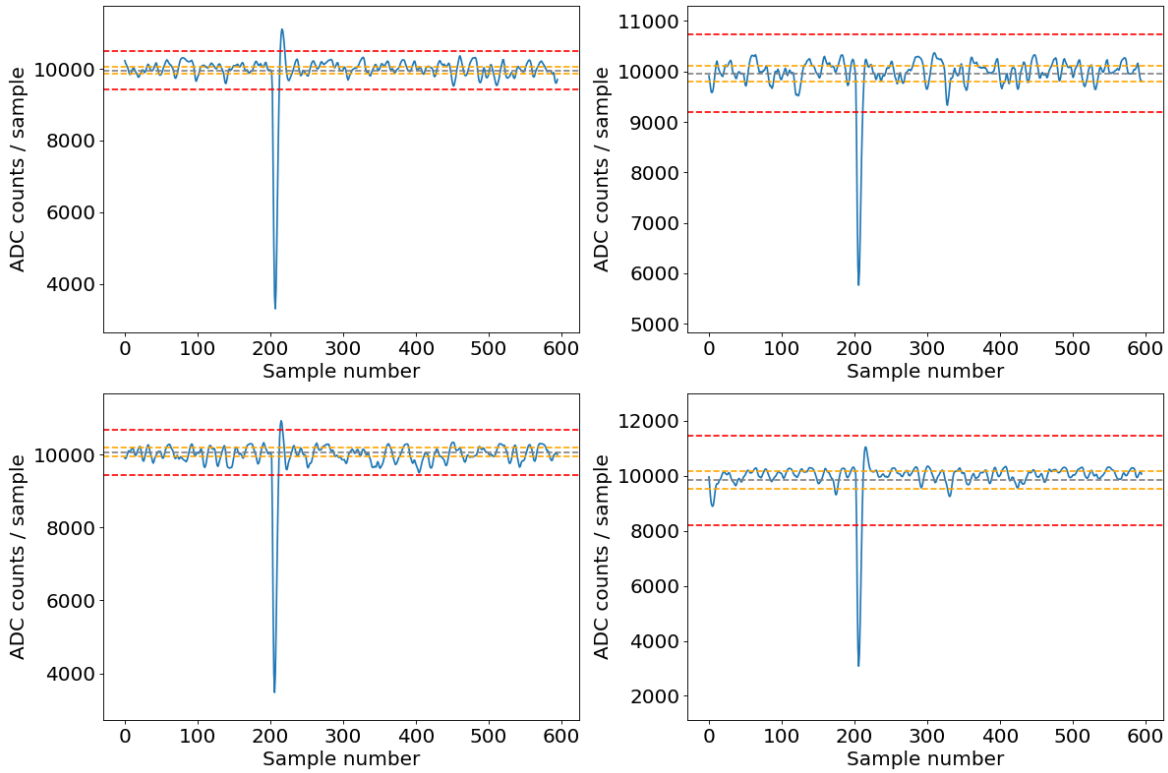


**Figure 46:** Waveforms of the four channels on the 16-channel readout PCB at room temperature, with a bias voltage of 56 V and LED amplitude of 2.4 V.

The uniformity in area and dimensions observed across all four channels confirms the operational functionality of the PCB at room temperature. The waveforms are comparable to the ones from the new PCB with only one signl readout, which was tested before. Notably, the waveforms from this test at room temperature display a secondary peak that overshoots into the positive region following the primary peak, a behavior not previously observed in other PCBs tested at room temperature, but only for the 16-channel readout PCB tested in a cold

environment.

The PCB's performance under cold conditions was then assessed. The temperature range studied was 170 K to 220 K, at intervals of 10 K. The waveforms at 220 K are displayed in Figure 47, captured with a bias voltage of 53.8 V and LED amplitude of 2.6 V in square pulses at a frequency of 100 Hz and a pulse width of 50 ns, ensuring a 5 V overvoltage on the PCB. Waveforms taken at other temperatures are not shown given their resemblance to the one presented.

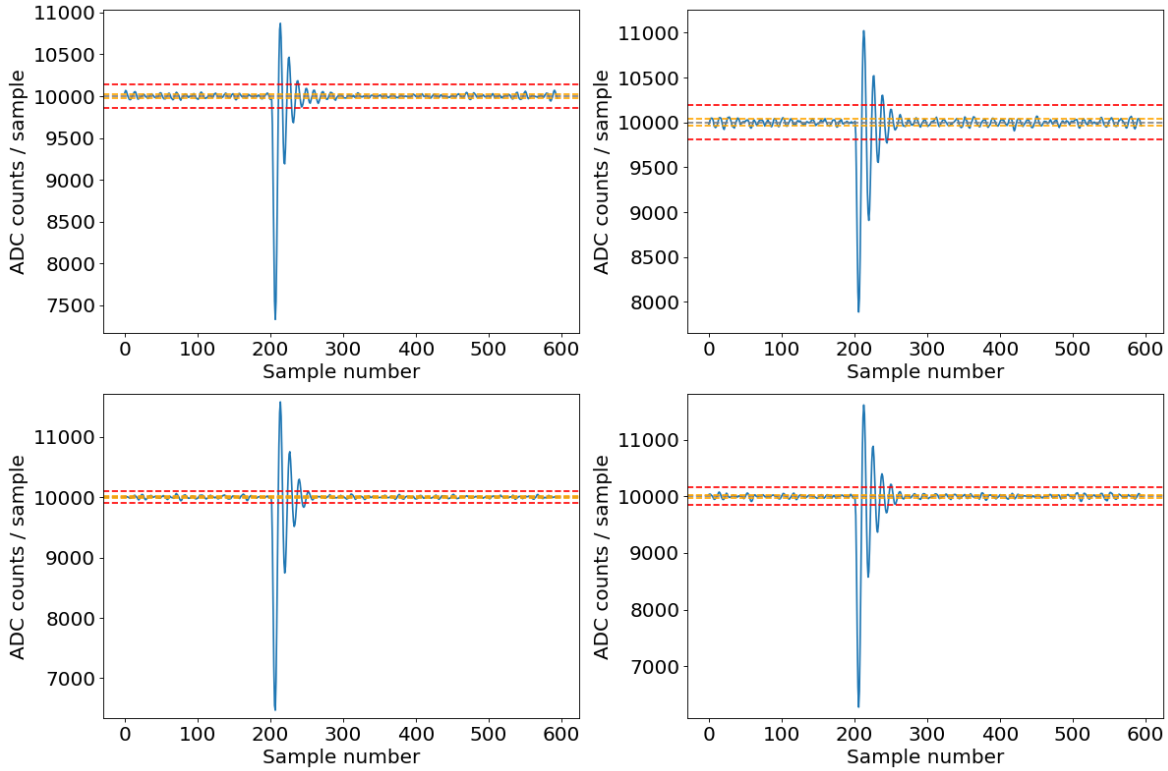


**Figure 47:** The waveforms at 220 K showing a ringing effect after the main signal peak, which suggests current backflow issues in the amplifying resistor.

Comparing these waveforms with those obtained at room temperature, a pronounced variation in shape is noticeable. The primary peak is followed by several smaller ones, showcasing a ringing effect. One possible cause might be the increased current in the amplifiers creating a reverse flow through the amplifying resistor. Installing a capacitor in parallel with the resistor could mitigate this effect. Despite this unforeseen behavior, the successful detection of signals from each SiPM unit confirms the effectiveness of the micro-coaxial cables in signal transmission from the PCB. Furthermore the ringing can be attributed to the new operational amplifiers and not the micro-coaxial cables, as an overshoot was already noticeable when using standard coax cables and the new operational amplifier. This advancement is a step towards higher granularity in readout and reduced total cabling mass.

# 6 Conclusion and Outlook

This thesis aimed to develop and characterize a new readout circuitry for the SiPM array in the dual-phase xenon TPC of Xenoscope, with a focus on improving the granularity of the photosensor array. The research involved testing of three different PCB designs: the original PCB equipped with operational-amplifier AMP-OPA847, a new PCB with operational-amplifier LTC6269-10, and a 16-channel readout PCB also incorporating the LTC6269-10, along with integrating micro-coaxial cables to enable compact signal readout.

The experimental setup for these tests spanned two configurations: Sandbox, used for room temperature measurements in a controlled dark setting, and LArS, used for measurements down to 170 K, simulating conditions closer to those of Xenoscope. These setups were important in evaluating the performance of the newly developed PCBs against the existing technology under identical testing conditions.

Comparative analysis between the original and new pre-amplifiers revealed that while the new LTC6269-10 op-amp demonstrates an ability to amplify signals with minimal loss even at LXe temperatures, characteristics of the SiPM such as DCR, CTP, BV, and Gain were comparable between both PCBs. Notably, there was a 4% to 6% loss in resolution at a gain of $10^6$, which is likely attributable to increased amplification noise. Additionally, in the 16-channel readout PCB design, a noticeable ringing effect was observed in the waveforms, characterized by several smaller peaks following the primary peak. This ringing could potentially be caused by increased current in the operational-amplifiers LTC6269-10, creating a reverse flow through the amplifying resistor. The overall integration of the compact pre-amplifier and micro-coaxial cables has proven effective, allowing the simultaneous readout of 16 signals.

For future work, the implementation of a capacitor in parallel to the feedback resistor on the LTC6269-10 op-amp circuits in the 16-channel readout PCB is planned. This adjustment aims to reduce the ringing effect observed at LXe temperatures, though its effectiveness remains to be tested. Further characterizations of the modified PCB will determine its practicality for future measurements.

The advancements made in this research enhance the granularity of the SiPM array in Xenoscope by integrating the new 16-channel readout PCB with LTC6269-10 operational amplifiers and micro-coaxial cables, which enable denser packaging and more precise signal readout. Finer granularity is of particular importance for experiments that require precise x-y position reconstruction. These improvements in sensor technology and readout precision provide a solid foundation for further developments in the field of particle physics, supporting the ongoing efforts to refine detection capabilities within the scope of the Xenoscope project.

# References


[1] F. Zwicky. "Die rotverschiebung von extragalaktischen nebeln". In: *Helvetica Physica Acta* 6 (1933), pp. 110–127.

[2] D. Yang and H.-B. Yu. "Self-interacting dark matter and small-scale gravitational lenses in galaxy clusters". In: *Physical Review D* 104.10 (2021), p. 103031.

[3] V. C. Rubin and W. K. Ford Jr. "Rotation of the Andromeda nebula from a spectroscopic survey of emission regions". In: *Astrophysical Journal* 159 (1970), p. 379.

[4] K. Begeman, A. Broeils, and R. Sanders. "Extended rotation curves of spiral galaxies: Dark haloes and modified dynamics". In: *Monthly Notices of the Royal Astronomical Society* 249.3 (1991), pp. 523–537.

[5] D. Clowe et al. "A direct empirical proof of the existence of dark matter". In: *The Astrophysical Journal* 648.2 (2006), p. L109.

[6] P. Collaboration et al. "Planck 2018 results". In: *A&a* 641 (2020), A12.

[7] J. Delabrouille et al. "The pre-launch Planck Sky Model: a model of sky emission at submillimetre to centimetre wavelengths". In: *Astronomy & Astrophysics* 553 (2013), A96.

[8] C. Armand and B. Herrmann. "Dark matter indirect detection limits from complete annihilation patterns". In: *Journal of Cosmology and Astroparticle Physics* 2022.11 (2022), p. 055.

[9] J. De Swart, G. Bertone, and J. van Dongen. "How dark matter came to matter". In: *Nature Astronomy* 1.3 (2017), p. 0059.

[10] L. Bergström. "Dark matter candidates". In: *New Journal of Physics* 11.10 (2009), p. 105006.

[11] G. Bertone and T. M. Tait. "A new era in the search for dark matter". In: *Nature* 562.7725 (2018), pp. 51–56.

[12] P. Bode, J. P. Ostriker, and N. Turok. "Halo formation in warm dark matter models". In: *The Astrophysical Journal* 556.1 (2001), p. 93.

[13] J. L. Feng. "Dark matter candidates from particle physics and methods of detection". In: *Annual Review of Astronomy and Astrophysics* 48 (2010), pp. 495–545.

[14] T. Bringmann and S. Hofmann. "Thermal decoupling of WIMPs from first principles". In: *Journal of Cosmology and Astroparticle Physics* 2007.04 (2007), p. 016.

[15] J. L. Feng. "The WIMP paradigm: Theme and variations". In: *SciPost Physics Lecture Notes* (2023), p. 071.

[16] G. Steigman, B. Dasgupta, and J. F. Beacom. "Precise relic WIMP abundance and its impact on searches for dark matter annihilation". In: *Physical Review D* 86.2 (2012), p. 023506.

[17] M. Battaglia et al. "Contrasting supersymmetry and universal extra dimensions at colliders". In: *arXiv preprint hep-ph/0507284* (2005).

[18] J. Billard et al. "Direct detection of dark matter—APPEC committee report". In: *Reports on Progress in Physics* 85.5 (2022), p. 056201.

[19] D. A. Bauer. "Dark matter detection with cryogenic detectors". In: *Journal of Physics: Conference Series*. Vol. 120. 4. IOP Publishing. 2008, p. 042002.

[20] M. Misiaszek and N. Rossi. "Direct detection of dark matter: a critical review". In: *arXiv preprint arXiv:2310.20472* (2023).

[21] C. Pérez de los Heros. "Status, challenges and directions in indirect dark matter searches". In: *Symmetry* 12.10 (2020), p. 1648.
[22] R. K. Leane. "Indirect detection of dark matter in the galaxy". In: *arXiv preprint arXiv:2006.00513* (2020).
[23] T. Slatyer. "Les Houches Lectures on Indirect Detection of Dark Matter". In: *arXiv preprint arXiv:2109.02696* 2109 ().
[24] L. Bergström. *Dark matter evidence, particle physics candidates and detection methods*. 2012.
[25] J. Aalbers et al. "DARWIN: towards the ultimate dark matter detector". In: *Journal of Cosmology and Astroparticle Physics* 2016.11 (2016), p. 017.
[26] E. Aprile et al. "Search for new physics in electronic recoil data from XENONnT". In: *Physical review letters* 129.16 (2022), p. 161805.
[27] J. Aalbers et al. "First dark matter search results from the LUX-ZEPLIN (LZ) experiment". In: *Physical review letters* 131.4 (2023), p. 041002.
[28] J. Aalbers et al. "A next-generation liquid xenon observatory for dark matter and neutrino physics". In: *Journal of Physics G: Nuclear and Particle Physics* 50.1 (2022), p. 013001.
[29] Y. Meng et al. "Dark matter search results from the PandaX-4T commissioning run". In: *Physical Review Letters* 127.26 (2021), p. 261802.
[30] T. Doke et al. "Absolute scintillation yields in liquid argon and xenon for various particles". In: *Japanese journal of applied physics* 41.3R (2002), p. 1538.
[31] L. Baudis et al. "A dual-phase xenon TPC for scintillation and ionisation yield measurements in liquid xenon". In: *The European Physical Journal C* 78 (2018), pp. 1–11.
[32] L. Baudis. "Dual-phase xenon time projection chambers for rare-event searches". In: *Philosophical Transactions of the Royal Society A* 382.2266 (2024), p. 20230083.
[33] E. Aprile et al. "Energy resolution and linearity of XENON1T in the MeV energy range". In: *The European Physical Journal C* 80 (2020), pp. 1–9.
[34] M. Schumann. *DARWIN - Dark Matter WIMP Search With Liquid Xenon — darwin.physik.uzh.ch*. https://darwin.physik.uzh.ch/darwin.html. [Accessed 16-04-2024].
[35] L. Baudis. "DARWIN/XLZD: A future xenon observatory for dark matter and other rare interactions". In: *Nuclear Physics B* 1003 (2024), p. 116473.
[36] P. Cushman et al. *Working group report: WIMP dark matter direct detection*. Tech. rep. Fermi National Accelerator Lab.(FNAL), Batavia, IL (United States), 2013.
[37] E. Aprile et al. "Projected WIMP sensitivity of the XENONnT dark matter experiment". In: *Journal of Cosmology and Astroparticle Physics* 2020.11 (2020), p. 031.
[38] E. Aprile et al. "First dark matter search with nuclear recoils from the XENONnT experiment". In: *Physical review letters* 131.4 (2023), p. 041003.
[39] L. Baudis et al. "Design and construction of Xenoscope—a full-scale vertical demonstrator for the DARWIN observatory". In: *Journal of Instrumentation* 16.08 (2021), P08052.
[40] R. Peres et al. "SiPM array of Xenoscope, a full-scale DARWIN vertical demonstrator". In: *Journal of Instrumentation* 18.03 (2023), p. C03027.

[41] L. Baudis et al. “The first dual-phase xenon TPC equipped with silicon photomultipliers and characterisation with 37Ar”. In: *The European Physical Journal C* 80.5 (2020), p. 477.

[42] R. J. M. Peres. “Advancing Multi-messenger Astrophysics and Dark Matter Searches with XENONnT and the Top SiPM Array of Xenoscope”. PhD thesis. Universität Zürich, 2023.

[43] *THE IDEAL PN JUNCTION AT EQUILIBRIUM — ebrary.net*. https://ebrary.net/158492/mathematics/ideal_junction_equilibrium. [Accessed 16-04-2024].

[44] *What is a SiPM and how does it work? | Hamamatsu Photonics — hub.hamamatsu.com*. https://hub.hamamatsu.com/us/en/technical-notes/mppc-sipms/what-is-an-SiPM-and-how-does-it-work.html. [Accessed 16-04-2024].

[45] S. Gundacker and A. Heering. “The silicon photomultiplier: fundamentals and applications of a modern solid-state photon detector”. In: *Physics in Medicine & Biology* 65.17 (2020), 17TR01.

[46] L. Baudis et al. “Characterisation of Silicon Photomultipliers for liquid xenon detectors”. In: *Journal of Instrumentation* 13.10 (2018), P10022.

[47] *Low light detection: PMT v. SiPM | Hamamatsu Photonics — hamamatsu.com*. https://www.hamamatsu.com/eu/en/resources/webinars/detectors/low-light-detection-pmt-sipm.html. [Accessed 16-04-2024].

[48] P. Hallen. “Determination of the Recovery Time of Silicon Photomultipliers”. In: *RWTH Aachen University* (2011).

[49] J. Haas. *Characterisation of Silicon Photomultipliers for Xenoscope*. https://www.physik.uzh.ch/dam/jcr:8b4bfa1b-68ce-43ee-96cc-066ffaf4aff7/Bachelor_thesis_Julian_Haas.pdf. [Accessed 16-04-2024]. 2023.

[50] F. Girard, K. Thieme, and J. Wulf. *DAQ*. https://github.com/Physik-Institut-UZH/DAQ, 2020.

[51] G. Gallina et al. “Characterization of the Hamamatsu VUV4 MPPCs for nEXO”. In: *Nuclear Instruments and Methods in Physics Research Section A: Accelerators, Spectrometers, Detectors and Associated Equipment* 940 (2019), pp. 371–379.